In situ NIR-IIb imaging of endogenous H_2S signaling for high-resolution abiotic stress visualization in plants

Feng *et al.*

Supplementary Method 1. Materials and characterization

Materials and chemical reagents

Lanthanide (III) acetate compounds, $Er(CH_3COO)_3$, $Nd(CH_3COO)_3$, $Ce(CH_3COO)_3$, $Yb(CH_3COO)_3$, and $Gd(CH_3COO)_3$, ammonium fluoride (NH_4F), 1-octadecene (ODE), hydrogen peroxide (H_2O_2), oleic acid (OA), 1-ethyl-3- (3-dimethylaminopropyl)carbodiimide (EDC), *N*-hydroxysuccinimide (NHS), 2',7'-dichlorodihydrofluorescein diacetate (DCFH-DA), MES monohydrate, salicylic acid (SA), 3-indoleacetic acid (IAA), and EDTA-2Na were acquired from Sigma-Aldrich Trading Co., Ltd (Shanghai, China). Thiobarbituric acid (TBA), trichloroacetic acid (TCA), 4',6-diamidino-2-phenylindole (DAPI), propidium iodide (PI), chlorophyll, lutein, cadmium chloride ($CdCl_2$), and 3,3',5,5'-tetramethylbenzidine (TMB) were obtained from Aladdin Biochemical Technology Co., Ltd (Shanghai, China). Polyethyleneimine (PEI), 3,3'-diaminobenzidine (DAB), Evans blue, reduced glutathione (GSH), L-ascorbic acid (AsA), sodium sulfide (Na_2S), horseradish peroxidase, and nitrotetrazolium blue chloride (NBT) were purchased from Macklin Biochemical Technology Co., Ltd (Shanghai, China). IR-820-$(COOH)_2$ was acquired from HEOWNS Biochem Technology LLC Co., Ltd (Tianjin, China). Hydrochloric acid (HCl), sodium hydroxide (NaOH), Evans Blue, Coomassie brilliant blue G250 (CBB G250), dithiothreitol (DTT), iron (III) chloride ($FeCl_3$), *N, N*-dimethyl-p-phenylenediamine (DPD), sulfuric acid (H_2SO_4), acetone, cyclohexane, ethanol, and glucose (GLU) were purchased from Sinopharm Chemical Reagent Co., Ltd. Titanium (IV) sulfate ($Ti(SO_4)_2$), ninhydrin, 2, 6-dichlorophenolindophenol (DCPIP), and L-cysteine (L-Cys) were obtained from Shanghai Dibai Biotechnology Co., Ltd. WSP-5 was purchased from TargetMol Chemicals Inc. The remaining chemical reagents and materials used in this study were purchased from legitimate local sources.

Materials characterization

The morphology and crystal structure of down-shifting nanoparticles (DSNPs) were characterized using transmission electron microscopy (TEM, HITACHI, HT-7820), high-resolution transmission electron microscopy (HRTEM, JEM-2100plus), and X-ray diffraction (XRD, Bruker D8 Advance). The chemical structure and zeta potential of the nanocomposites were analyzed with a Fourier-transform infrared (FT-IR) spectrometer (Thermo Fisher Scientific, Nicolet iS10) and a nanosizer and zeta potential analyzer (Zetasizer

Nano ZS90), respectively. The absorption spectrum of the nanoprobes was recorded using a UV-Vis-NIR spectrophotometer (PerkinElmer Lambda 950). Fluorescence emission spectra in the UV-Vis and NIR-II regions were measured with a fluorescence spectrophotometer (HITACHI, F-4500) and a near-infrared fluorescence microscopy imaging system (Princeton Instruments, NIRvana 640LN), respectively. Fluorescence images in the UV-Vis region were captured using the IVIS Spectrum imaging system (PerkinElmer).

Supplementary Method 2. Fabrication of nanocomposites

Fabrication of $NaGdF_4$:Yb,Er,Ce@$NaGdF_4$:Yb,Nd@PEI

The surface ligands of $NaGdF_4$:Yb,Er,Ce@$NaGdF_4$:Yb,Nd were removed through acetone precipitation and acid washing (hydrochloric acid, HCl, 36%)[1]. The resulting nanoparticles were then dissolved in ethanol. Under ultrasonication, a solution of PEI (0.6 mL, 20.0 mg mL^{-1}) was continuously added to the above system. The reaction mixture was stirred at room temperature for 12 h. Subsequently, the mixture was subjected to centrifugation (36700 × g for 20 min) and washed with water to remove excess PEI, yielding PEI-functionalized lanthanide nanoparticles.

Fabrication of $NaGdF_4$:Yb,Er,Ce@$NaGdF_4$:Yb,Nd@PEI-820 nanocomposites

N-hydroxysuccinimide (NHS) (0.05 mM) and 1-ethyl-3-(3-dimethylaminopropyl)carbodiimide (EDC) (0.05 mM) were dissolved in ethanol. Subsequently, IR-820-$(COOH)_2$ was added to the mixture, which was stirred for 2 h[2]. The PEI-modified lanthanide nanoparticles were then introduced into the system and stirred for an additional 12 h. Lastly, the mixture was subjected to centrifugation (36700 × g for 20 min), followed by washing with water and ethanol to remove any unreacted components.

Supplementary Method 3. Evaluation of anti-interference performance

The effects of common interferents in plant biological matrices on the signal intensity of IR-820-$(COOH)_2$ and the nanoprobe were investigated. These interferents included metal ions (Na^+, K^+, Fe^{3+}, Mg^{2+}), anions (Cl^-, HCO^{3-}, NO^{3-}, PO_4^{3-}, SO_4^{2-}, SO_3^{2-}, HSO_3^-, $S_2O_3^{2-}$, $S_2O_5^{2-}$), biothiols (D-Cys, L-Cys, GSH), plant hormones (SA, IAA), ROS (H_2O_2, •OH, $•O_2^-$, and $^1O_2$), and other metabolic regulatory molecules (AsA, GLU, NO). Each

interferent was individually added to solutions of IR-820-$(COOH)_2$ or the as-prepared nanoprobes at concentrations comparable to or exceeding their typical physiological levels in plant tissues. Specifically, the assay concentrations were as follows: 400 mM for K^+; 300 mM for Cl^-; 200 mM for Na^+; 100 mM for glucose; 50 mM for Mg^{2+}, HCO_3^-, NO_3^-, and PO_4^{3-}; 10 mM for GSH and SO_4^{2-}; 1.0 mM for Fe^{3+}, $S_2O_3^{2-}$, SO_3^{2-}, and HSO_3^-; and 100 μM for $S_2O_5^{2-}$, D-Cys, L-Cys, SA, IAA, H_2O_2, AsA, as well as donors of NO, $\bullet O_2^-$, $^1O_2$, and •OH.

Supplementary Method 4. Determination of stress-related physiological and biochemical parameters in plant leaves

Determination of H_2O_2 levels in leaves

The quantification of H_2O_2 in plant tissues was performed via reaction with $Ti(SO_4)_2$, which produces a yellow titanium peroxide exhibiting an absorption maximum at 410 nm[3]. Typically, a mixture consisting of 1.0 g of plant leaf, which had been rapidly frozen in liquid nitrogen, and 1 mL of pre-cooled acetone was prepared. After adding quartz sand to the mixture, it was thoroughly ground to create a tissue homogenate. The mixture was then centrifuged at 7100 × g for 15 min at 4 °C. Subsequently, 0.5 mL of the supernatant was collected and mixed with 0.05 mL of 5% $Ti(SO_4)_2$ and 0.1 mL of ammonium hydroxide. Following precipitation, the mixture was centrifuged at 7100 × g for 3 min at 4 °C. The supernatant was discarded, and the residue was washed with acetone to remove pigments. Finally, 2.5 mL of 2 M H_2SO_4 was added to the mixture to dissolve the pale yellow precipitate, and the absorbance of the solution was measured at 410 nm.

Determination of H_2S levels in leaves

H_2S quantification was conducted using the methylene blue method. Briefly, acid-liberated H_2S was captured with zinc acetate and reacted with DPD in the presence of $FeCl_3$, generating a methylene blue derivative measured at 670 nm[4]. Specifically, 0.1 g of leaf tissue was added to 0.9 mL of pre-cooled Tris-HCl buffer (pH 8.0, containing 10 mM EDTA) and ground into a homogenate under liquid nitrogen. The homogenate was then centrifuged at 15800 × g for 10 min at 4 °C, and the supernatant was collected. After adding 0.5 mL of hydrochloric acid (1 M), the mixture was placed in a closed system. Subsequently, 0.5 mL of zinc acetate solution

(1%) was added, and the mixture was incubated at 37 °C for 40 min. Finally, 100 μL of $FeCl_3$ (30 mM) and 100 μL of DPD (20 mM) were added to the mixture, and the absorbance of the solution was measured at 670 nm.

Determination of proline levels in leaves

The quantification of proline in plant tissues was performed via reaction with ninhydrin under acidic conditions, which produces a red chromophore exhibiting an absorption maximum at 520 nm[5]. Briefly, 0.2 g of leaf tissue was added to 2 mL of 3% sulfosalicylic acid and ground into a homogenate using liquid nitrogen. The homogenate was then boiled for 10 min. After cooling to room temperature, the mixture was centrifuged at 1000 × g for 10 min. Subsequently, 1 mL of the supernatant was collected and mixed with 1 mL of 3% sulfosalicylic acid, 1 mL of glacial acetic acid, and 2 mL of 2.5% ninhydrin. The mixture was placed in a boiling water bath for 1 h. After cooling, 2 mL of toluene was added to the solution, which was then shaken to facilitate extraction. The absorbance of the solution was measured at 520 nm.

Determination of AsA levels in leaves

The quantification of ascorbic acid (AsA) in plant tissues was performed via redox titration with DCPIP under acidic conditions, which produces a decolorization endpoint upon complete oxidation of AsA. Typically, 10 g of leaf tissue was added to a 2% oxalic acid solution and ground into a homogenate using liquid nitrogen. The homogenate was then diluted to a final volume of 100 mL with the oxalic acid solution. The mixture was thoroughly mixed, extracted for 15 min, and filtered to collect the solution. Subsequently, 10 mL of the extract was taken and titrated with a standardized 2,6-dichlorophenolindophenol solution until a pink endpoint was reached. The AsA content in the leaves was calculated based on the previously determined titration factor.

Determination of MDA levels in leaves

The quantification of malondialdehyde (MDA) in plant tissues was performed via reaction with TBA under acidic conditions, which produces a pink chromophore exhibiting characteristic absorption at 532 nm. Specifically, a mixture of 0.2 g of leaf tissue and 2 mL of 5% TCA was ground in liquid nitrogen to form a homogenate. The mixture was then centrifuged at 1000 × g for 10 min at 4 °C, and 2 mL of the supernatant was

carefully collected. Subsequently, 2 mL of 0.67% TBA was added to the solution, and the mixture was boiled at 100 °C for 15 min. After centrifugation at 1000 × g for 10 min, the absorbance of the resulting solution was measured at 450 nm, 532 nm, and 600 nm[6]. The MDA content of the leaf tissue was calculated using the following equation:

$$6.45 \times (A_{532} - A_{660}) - 0.56 \times A_{450} \quad (1)$$

Determination of the total antioxidant capacity (TAOC) of leaves

A total of 0.1 g of leaf tissue was added to pre-cooled phosphate-buffered saline (PBS) buffer at pH 5.5 and ground into a homogenate under liquid nitrogen. The homogenate was then diluted with PBS solution until it reached an almost colorless appearance. Subsequently, 50 μL of the diluted solution was added to a mixture containing horseradish peroxidase (HRP) at a concentration of 0.05 U mL^{-1}, tetramethylbenzidine (TMB) at 0.5 mM, and H_2O_2 at 0.5 mM. Then, the mixture was incubated at room temperature for 15 min. The absorbance of the resulting solution was measured at 652 nm. AsA was used as the standard antioxidant to establish the standard curve, and the TAOC of leaf tissues was ultimately expressed as AsA equivalents[7,8].

Measurement of leaf relative electric conductivity

The relative electrical conductivity (REC) of leaf tissues was determined using a conductivity meter (FiveEasy Plus, Mettler Toledo)[6]. Briefly, a fixed area of plant tissue was punched from the leaf and completely immersed in 10 mL of deionized water. The system was then placed on a shaker at room temperature for 12 h. A boiling water bath (15 min) and deionized water were set as the positive (EC_1) and negative controls (EC_2), respectively. The electrical conductivity (EC) of the tissue after soaking was measured using a conductivity meter, and the REC of the tissue was calculated using the following formula:

$$REC = (EC - EC_2) / EC_1 \quad (2)$$

Determination of leaf chlorophyll and nitrogen content

Briefly, foliar relative chlorophyll content (SPAD value) and nitrogen nutritional status were measured using a portable chlorophyll meter (TOP Cloud-agri, TYS-4N).

Determination of L-cysteine desulfurylase activity in leaves

L-cysteine desulfurylase (LCD) activity was determined by quantifying H_2S production from the enzymatic desulfuration of L-Cys, where LCD catalyzes the conversion of L-Cys to H_2S, pyruvate, and ammonium[9]. Specifically, 0.2 g of leaf tissue was added to 1.0 mL of Tris-HCl buffer (pH 8.0, 20 mM) and ground into a homogenate under liquid nitrogen. The homogenate was then centrifuged (15800 × g, 10 min, 4 °C), and the supernatant was collected. The protein concentration in the supernatant was adjusted to 100 μg mL^{-1} using CBB G250. Subsequently, 100 μL of the adjusted supernatant was added to a mixture containing 100 μL of L-Cys (0.8 mM), 400 μL of DTT (2.5 mM), and 400 μL of Tris-HCl buffer (pH 9.0, 20 mM). The mixture was incubated at 37 °C for 45 min. After incubation, 100 μL of $FeCl_3$ (30 mM) and 100 μL of DPD (20 mM) were added to the solution. The generation of H_2S was measured using the same protocol as described in section "Determination of H_2S levels in leaves". The activity of LCDs in the leaf tissue was assessed by evaluating the level of H_2S produced.

Determination of oxidoreductase activity in plant leaves

Before determining the activity of the antioxidant enzyme, 0.2 g of the plant sample was added to 1 mL of PBS at pH 7.0, containing 0.1 mM EDTA, and quickly frozen in liquid nitrogen. The mixture was then ground to create a homogeneous tissue homogenate. Subsequently, the homogenate was centrifuged at 1000 × g for 30 min at 4 °C, and the supernatant was collected as the extracted enzyme solution. Additionally, the protein content of the enzyme solution was adjusted to 100 μg mL^{-1} using a CBB G250 to standardize the oxidoreductase activity[3,10].

To determine the activity of CAT, 100 μL of a standardized enzyme solution, 4.8 mL of PBS buffer (pH 7.0, containing 0.1 mM EDTA), and 100 μL of H_2O_2 (80 mM) were mixed and incubated at 37 °C. CAT catalyzes the decomposition of H_2O_2 into H_2O and O_2. Therefore, the activity of CAT was assessed by measuring the amount of O_2 generated in each system using a dissolved oxygen analyzer (REX, PB-607A)[11–13].

To determine the activity of APX, 100 μL of a standardized enzyme solution, 100 μL of ascorbic acid (AsA, 30 mM), 4.7 mL of PBS buffer at pH 7.0 containing 0.1 mM EDTA, and 100 μL of H_2O_2 (20 mM) were mixed and incubated at 37 °C. Subsequently, the absorbance of each mixture at 290 nm was rapidly recorded using a UV-Vis spectrophotometer to calculate the remaining amount of AsA, which in turn reflects the activity of APX[3].
To determine the activity of POD, 100 μL of a standardized enzyme solution, 10 μL of H_2O_2 (10 mM), 4.88 mL of PBS buffer (pH 5.5), and 10 μL of TMB (200 mM) were mixed and incubated at 37 °C. Subsequently, the absorbance of each mixture was rapidly recorded at 652 nm using a UV-Vis spectrophotometer[14,15].

Additionally, the SOD activity and GSH content in the leaves were determined using an SOD Activity Assay Kit (Abbkine Scientific, Wuhan, China) and a Reduced GSH Detection Kit (Abbkine Scientific, Wuhan, China), respectively.

Supplementary Method 5. In planta evaluation and validation of DSNPs@PEI-820 for H_2S imaging

Metabolism and tissue distribution of DSNPs@PEI-820 following *in situ* leaf injection

DSNPs@PEI-820 was introduced into defined regions of lettuce and tobacco leaves via needle-free injection. The distribution of the nanoprobes was monitored for up to 60 h after delivery. Fluorescence imaging was performed at both microscopic and macroscopic levels to evaluate the spatial distribution, transport, and tissue localization of the nanoprobes. Fluorescence signals were recorded from the injection site, adjacent leaf tissues, veins, stems, and roots at designated time points.

Root-mediated delivery of DSNPs@PEI-820 and imaging of stress-induced H_2S signals in roots

Hydroponically grown lettuce plants were incubated in an MES solution containing DSNPs@PEI-820 for 8 h under standard growth conditions to evaluate root-mediated uptake and translocation. NIR-IIb fluorescence images were acquired at designated time points to monitor the distribution of the nanoprobes within roots, stems, and leaves. For imaging Cd^{2+}-induced H_2S generation, lettuce plants preloaded with DSNPs@PEI-820 via root absorption were subjected to Cd^{2+} stress. Fluorescence images were recorded under 808 nm and 980 nm

excitation at different stress durations, and the corresponding ratiometric signals (I_{808}/I_{980}) were calculated. Endogenous H_2S concentrations in root tissues were determined using the standard methylene blue assay.

In-tissue calibration of DSNPs@PEI-820 for H_2S detection

To construct *in vivo* calibration curves, DSNPs@PEI-820 was infiltrated into the leaves of lettuce (0.26 mm thickness) and tobacco (0.39 mm thickness) via a needle-free method. Following probe infiltration, varying concentrations of exogenous H_2S (0–50 μM) were sequentially injected *in situ* into the same leaf region. After incubation, fluorescence images were acquired under 808 nm and 980 nm excitation, and the corresponding ratiometric fluorescence signals were calculated to establish the in-tissue calibration curves.

Photophysical stability and ratiometric robustness of DSNPs@PEI-820

DSNPs@PEI-820 were evaluated *in vitro* by co-incubation with a simulated leaf tissue homogenate and *in vivo* via needle-free leaf infiltration. Experiments were performed in both unreacted and H_2S-activated states. Fluorescence intensities under 808 nm and 980 nm excitation were measured across laser power ranges of 4.04–10.84 mW cm^{-2} and 5.08–13.63 mW cm^{-2}, respectively. Both absolute (F_p) and power-normalized (F_p/P) intensities were recorded, and ratiometric signals (I_{808}/I_{980}) were calculated.

Spatial mapping of H_2S distribution via confocal fluorescence imaging

Lettuce leaf tissues subjected to varying concentrations of Cd^{2+} stress (0–1.0 mM) were excised and immediately immersed in a WSP-5 working solution (25 μM in MES buffer containing 1% DMSO) and incubated for 30 min at 25 °C in darkness. To facilitate uniform dye penetration throughout the leaf tissues, the samples were subjected to vacuum infiltration. Following staining, excess dye on the tissue surface was thoroughly removed by washing with MES buffer. The processed tissues were then mounted on glass slides and imaged using an ultra-high-resolution confocal laser scanning microscope (LSM 980 with Airyscan, Zeiss, Germany) to precisely record the spatial distribution of H_2S signals within intracellular and extracellular compartments. Semi-quantitative analysis of region-specific fluorescence intensities was performed using ZEN 3.11 and ImageJ software.

Evaluation of infiltration-induced signals

Healthy lettuce leaves were used to evaluate background signal fluctuations induced by the delivery process. DSNPs@PEI-820 nanoprobes suspended in MES buffer were delivered into the leaf tissues via needle-free infiltration. Immediately after infiltration, dynamic NIR-II fluorescence signals in the infiltrated regions were continuously monitored using an InGaAs imaging system. To clearly distinguish infiltration-induced background signal from genuine stress responses, a parallel group was included in which mechanical wounding stress was applied to the leaves 60 min after the initial infiltration. In parallel, time-dependent colorimetric assays were performed to quantify fluctuations in endogenous H_2S and H_2O_2 levels within the infiltrated regions across different treatment groups, including DSNPs@PEI-820 nanoprobes in MES buffer, MES buffer only, and untreated controls.

Biochemical validation of *in vivo* H_2S specificity via L-CDes inhibition

Prior to experimentation, lettuce plants were transferred to a modified Hoagland nutrient solution and acclimated for 24 h. Subsequently, the plants were exposed to Cd^{2+} stress, with co-treatments of varying concentrations of hydroxylamine (HA; 0–800 μM). Following these treatments, DSNPs@PEI-820 nanoprobes were delivered into the leaf tissues of each group via needle-free infiltration. After a designated co-incubation period, the leaf tissues were freshly excised and immediately visualized using a NIR-II fluorescence microscope to monitor localized signal intensity.

Supplementary Method 6. Histochemical and fluorescence staining of plant leaf tissues

Reactive oxygen species staining in leaf tissue

DCFH-DA staining of leaves: to visualize ROS in plant leaves, leaves subjected to various treatments were fully immersed in a DCFH-DA solution (50 μM). A vacuum was applied for 3 min to enhance dye penetration, followed by incubation in the dark at room temperature for 30 min. Subsequently, the leaves were thoroughly washed with MES buffer to remove any residual dye and were then observed under a fluorescence microscope [16].

Detection of H_2O_2 and $\bullet O_2^-$ in plant leaves: The distribution of H_2O_2 and $\bullet O_2^-$ in plant leaves under stress was characterized using DAB and NBT staining, respectively[3,16,17]. A series of treated leaves was completely immersed in DAB (0.1%, containing Tween-20) and NBT (0.05%) solutions. A vacuum was applied for 3 min to enhance dye penetration. The leaves were stained in the dark for 12 h and then fully decolorized using boiling ethanol. Finally, the stained leaves were fixed in a mixture of anhydrous ethanol, 85% lactic acid, and glycerol in a volume ratio of 3:1:1. Microscopic images of the stained tissues were captured using an optical microscope.

DAPI/PI and Evans blue staining of leaves

Live/dead cell staining: Leaves were fixed in 4% paraformaldehyde for 2 h. Subsequently, leaves subjected to various treatments were sequentially immersed in DAPI (5 μg mL^{-1} for 10 min) and PI (10 μg mL^{-1} for 10 min)[18–20]. The samples were then incubated in the dark at room temperature for 20 min. After incubation, the leaves were thoroughly washed with MES buffer to remove residual dyes and were observed under a fluorescence microscope.

Evans blue staining for membrane integrity under stress: A series of leaves subjected to various treatments were completely immersed in a 0.25% Evans blue solution and stained in the dark for 24 h[17]. The leaves were then thoroughly washed with MES buffer to remove any residual dye. Subsequently, a mixture of ethanol and glycerol (in a 9:1 volume ratio) was boiled to fully decolorize the leaves. Finally, Evans blue was extracted from the leaves using a 1% SDS aqueous solution, and the absorbance of the resulting solution was measured at 600 nm.

Supplementary Method 7. Density functional theory calculations

This study employed density functional theory (DFT) to investigate the molecular structures and Gibbs free energies of dye molecules. All quantum chemical calculations were performed using ORCA 6.0[21–24], with geometry optimizations conducted at the B3LYP-D3/def2-SVP level of theory[25–27]. An implicit solvation model was applied to account for the effects of an aqueous solvent[28]. Molecular electrostatic potential analysis was carried out using Multiwfn 3.8 (dev)[29,30], and visualization was conducted with VMD[31] and VESTA[32].

Supplementary Note 1. Elemental distribution characterization of core-shell nanostructures

The core–shell nanoarchitecture and elemental distribution of the DSNPs were rigorously validated using energy-dispersive spectroscopy (EDS) line-scanning. EDS line-scanning revealed well-defined spatial distributions of lanthanide ions, with Gd and Yb present across both core and shell regions, whereas Er and Ce were confined to the core (Supplementary Fig. 6). The spatially resolved elemental profiling provides compelling evidence for the construction of the designed $NaGdF_4$:Yb,Er,Ce@$NaGdF_4$:Yb,Nd nanostructure with precisely controlled lanthanide ion localization.

Supplementary Note 2. Characterization of Ce^{3+} doping strategy for suppressing upconversion and promoting down-shifting emission in DSNPs

This mechanism was further confirmed through comparative fluorescence emission spectroscopy of nanocrystals with varying Ce^{3+} doping levels. Increasing Ce^{3+} concentration progressively suppressed the 541 nm upconversion emission and shortened its lifetime, while simultaneously increasing both the intensity and lifetime of the 1550 nm NIR-IIb emission. At a 5% Ce^{3+} doping level, the 1550 nm emission intensity markedly increased, from 27.16% at 0% Ce^{3+} to 82.13%, demonstrating highly efficient down-shifting enhancement (Supplementary Fig. 8). Therefore, 5% Ce^{3+} doping was identified as the optimal composition for practical imaging applications.

Supplementary Note 3. FT-IR characterization of surface bonding in DSNPs, DSNPs@PEI, and DSNPs@PEI-820

Compared with bare DSNPs, DSNPs@PEI exhibited a substantial decrease in the broad O–H/N–H stretching band (3200–3600 cm^{-1}) and a pronounced change in the N–H bending vibration at 1554 cm^{-1}, reflecting the presence of nitrogen-rich PEI on the nanoparticle surface. These spectral changes indicate that PEI interacts with DSNPs through coordination or hydrogen-bonding interactions. The covalent conjugation of IR-820-$(COOH)_2$ to the DSNPs was confirmed by the FT-IR spectra. The emergence of characteristic amide I (1643 cm^{-1}) and amide II (1556 cm^{-1}) bands, accompanied by a decrease in N–H stretching intensity (3200–3600 cm^{-1}), provides direct evidence of amide bond formation between dye carboxyl groups and PEI amines. Additional spectral

features, including enhanced absorption in the 1500–1730 cm^{-1} region attributable to benzoindole and carboxylate moieties, as well as distinct changes in the fingerprint region (650–680 cm^{-1}) and C–H stretching bands (2800–2950 cm^{-1}), further support the presence of covalently attached IR-820 derivatives on the nanoparticle surface (Supplementary Fig. 11).

Supplementary Note 4. XPS characterization of surface bonding in DSNPs@PEI and DSNPs@PEI-820

XPS analysis further confirmed the covalent coupling of IR-820-$(COOH)_2$ to the nanoparticle surface. In DSNPs@PEI-820, the N 1*s* spectrum displayed a newly emerged peak corresponding to amide nitrogen, while the O 1*s* spectrum showed distinct components attributable to carboxylic acid and amide carbonyl oxygen. These spectral features, absent or significantly weaker in DSNPs@PEI, provide strong evidence that IR-820-$(COOH)_2$ is covalently anchored to the nanoparticle surface through stable amide linkages (Supplementary Fig. 12).

Supplementary Note 5. Mechanistic characterization and DFT analysis of the nucleophilic addition reaction between IR-820-$(COOH)_2$ and H_2S

Supplementary Figs. 19a, b presented the HRMS results of IR-820-$(COOH)_2$ before and after reaction with S^{2-}. The product spectrum exhibited multiple fragment signals corresponding to thiolated IR-820-$(COOH)_2$ ions within the m/z range of 813.39 to 816.39, which closely align with our theoretical predictions (Supplementary Fig. 19c). FT-IR analysis of IR-820-$(COOH)_2$ thiol showed increased intensity and broadening of the main peak between 1520 and 1680 cm^{-1}, attributed to the disruption of the conjugated structure and the reduced molecular symmetry. Furthermore, concomitant increases at 2450–2550 cm^{-1} (−SH) and 630–670 cm^{-1} (C−S) confirmed thiol formation (Supplementary Fig. 19d). These characterization results validate the DFT-derived mechanism, confirming that H_2S nucleophilic addition disrupts the π-conjugation of IR-820-$(COOH)_2$ through structural modifications at the sp^3-hybridized carbons located between the benzoindolium units and the heptamethine bridge. The C−C bond adjacent to the addition site elongates from 1.40 Å to 1.49 Å, and the dihedral angle between the benzoindolium and heptamethine planes increases from −179.2° to −121.5° due to rotation around the sp^3-hybridized carbon (Fig. 3d). LUMO-HOMO calculations display an increased bandgap in IR-820-

$(COOH)_2$ thiol compared to IR-820-$(COOH)_2$, accounting for the attenuated intensity and blue shift of the main absorption peak. These results verify that H_2S addition disrupts the π-conjugated coplanarity of IR-820-$(COOH)_2$, causing a reduction in its absorption and fluorescence emission.

Supplementary Note 6. DFT investigation into the nucleophilic reaction mechanism of cyanine dyes with H_2S

Relative to other cyanine dyes, the extended conjugation of IR-820-$(COOH)_2$ increases positive electrostatic potential at the terminal $C=N^+$ group, making these iminium bonds the main sites for attack by H_2S and subsequent thiol-adduct formation via nucleophilic addition (Fig. 3b and Supplementary Fig. 20a). Frontier molecular orbital analysis further shows that IR-820-$(COOH)_2$ possesses a lower LUMO energy level and a narrower HOMO–LUMO gap than shorter-chain analogues, facilitating electron donation from the HOMO of H_2S and lowering the kinetic barrier for nucleophilic addition (Fig. 3c and Supplementary Fig. 20b).

Supplementary Note 7. Assessment of plant autofluorescence on tissue fluorescence imaging across different optical windows

Plant endogenous fluorophores have an important role in light capture, photoprotection, and stress responses. Here, we analyzed the autofluorescence profiles of dominant plant pigments (chlorophyll, lutein, and carotene) whose conjugated structures give rise to noticeable tissue autofluorescence under UV-visible imaging. As shown in Supplementary Figs. 28, 29a, under UV-visible excitation, chlorophyll produces fluorescence both in the visible and NIR windows, while carotenoids fluoresce only in the UV-visible range. To avoid the interference of chlorophyll, we also measured its fluorescence emission under 808 nm and 980 nm NIR excitation. The results showed negligible emission of chlorophyll at these wavelengths, consistent with NIR autofluorescence imaging of leaves (Supplementary Figs. 29b, 30).

Supplementary Note 8. Evaluation of the high-resolution imaging advantage of NIR-IIb-emitting probes in intact plant leaves

We further compared the performance of the probes loaded in capillaries beneath living lettuce and tobacco leaves with different thicknesses (Supplementary Fig. 32). The complicated microarchitecture of the leaves caused strong scattering of the visible and NIR-I fluorescence, resulting in large signal attenuation. In contrast, the NIR-IIb probe consistently exhibited high SBR as well as better spatial resolution for all leaf thicknesses due to its significantly reduced tissue scattering and absorption. These results validate the improved imaging fidelity and robustness of the probe in the real plant tissue environment.

Supplementary Note 9. Assessment of potential baseline interference caused by needle-free nanoprobe injection

Although the needle-free infiltration method induces a localized, transient stress signal at the injection site, this disturbance does not compromise the sensor's reliability. Specifically, H_2O_2 levels (a representative ROS) show a transient increase and return to physiological baseline within 1 h (Supplementary Fig. 36a). Similarly, the infiltration-induced fluctuations in H_2S are negligible compared to stress-induced bursts (Supplementary Fig. 36b). Importantly, these molecular events do not trigger false-positive signals, as both the baseline signal intensity and the SBR remain stable during this initial 1-h recovery period prior to further stress (Supplementary Fig. 37).

Supplementary Note 10. Temporal compatibility of DSNPs@PEI-820 for dynamic *in vivo* H_2S tracking

Furthermore, effective tracking of physiological signals requires temporal compatibility. The nucleophilic reaction kinetics of DSNPs@PEI-820 match the gradual time course of stress-induced H_2S generation. Time-course *in vivo* monitoring under Cd^{2+} exposure captured the dynamic trends of H_2S generation, consistent with standard biochemical measurements (Supplementary Fig. 53).

Supplementary Note 11. ROS staining of leaf tissue

Following DAB and NBT staining, most regions of the leaves in the stress groups exhibited elevated levels of H_2O_2 and $\bullet O_2^-$ compared to the control group (Supplementary Fig. 61). This indicated that the leaf tissues

experienced significant oxidative stress under stress. After DCFH-DA staining, guard cells in each stress group exhibited a bright green fluorescence, indicating significant oxidative stress (Supplementary Fig. 62).

Supplementary Note 12. Viability staining of leaf tissue under abiotic stress

DAPI/PI and Evans blue staining of stressed leaf tissues revealed that, compared to heat shock, both Cd^{2+} exposure and mechanical wounding caused more severe cellular membrane damage, leading to increased cellular apoptosis (Supplementary Fig. 63).

Supplementary Note 13. Characterization of REC, TAOC, and proline levels in leaf tissue under abiotic stress

The REC of plant tissues and proline content (essential for osmoregulation) exhibited significant increases. This indicated the loss of selective permeability in leaf cells. Meanwhile, the increase in leaf TAOC suggested that the antioxidant system of the tissue was activated under stress (Supplementary Fig. 65).

Supplementary Note 14. Characterization of H_2S distribution in leaf tissue under abiotic stress by Cu^{2+} staining

The leaf tissues of the stressed groups exhibited numerous dark brown products (CuS) resulting from the reaction of H_2S with indicator ions, indicating the formation and distribution of H_2S signaling molecules in leaves under stress conditions (Supplementary Fig. 67).

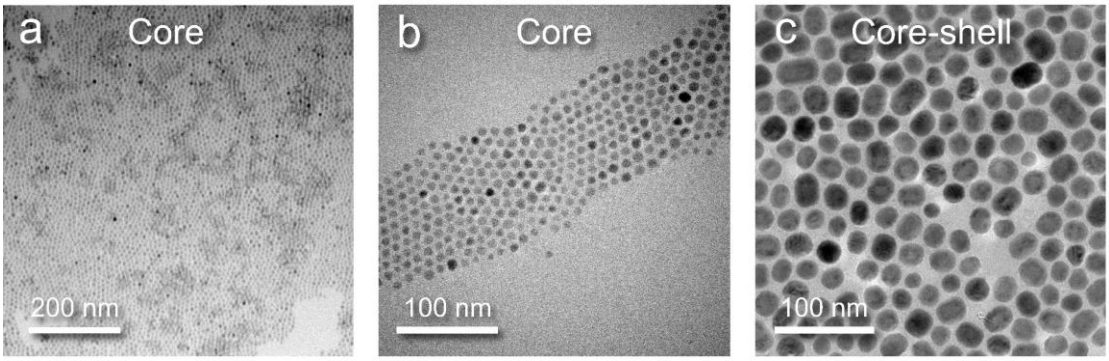

Supplementary Fig. 1. TEM images of core and core-shell DSNPs. TEM images of $NaGdF_4$:Yb,Er,Ce (a, b) and $NaGdF_4$:Yb,Er,Ce@$NaGdF_4$:Yb,Nd (c, in cyclohexane).

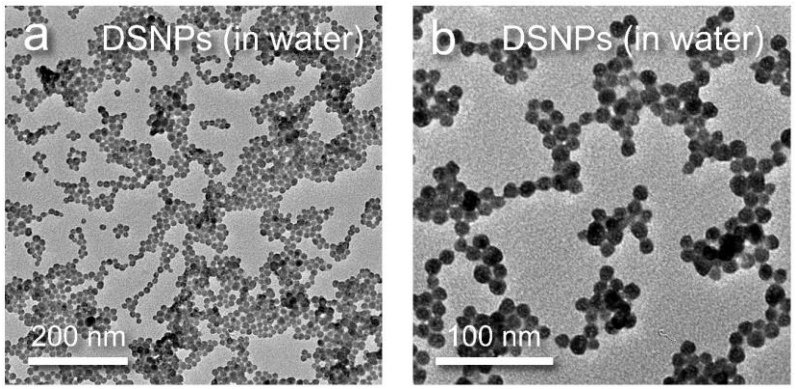

Supplementary Fig. 2. TEM image of water-soluble core-shell DSNPs. TEM image (a) and a local magnification (b) of water-soluble $NaGdF_4$:Yb,Er, Ce@$NaGdF_4$:Yb,Nd.

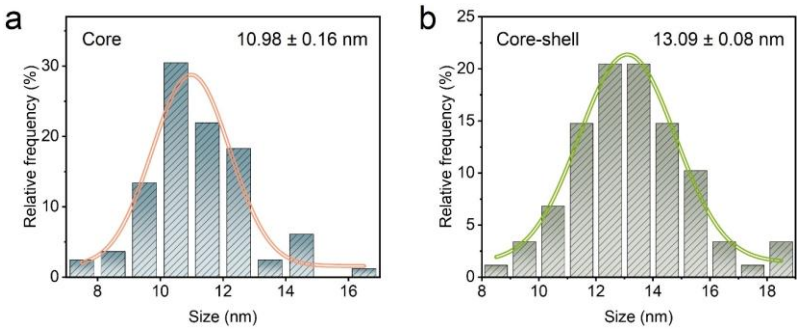

Supplementary Fig. 3. Particle size analysis of core and core-shell DSNPs. Particle size distribution of $NaGdF_4$:Yb,Er,Ce (a), $NaGdF_4$:Yb,Er,Ce@$NaGdF_4$:Yb,Nd (b). Source data are provided as a Source Data file.

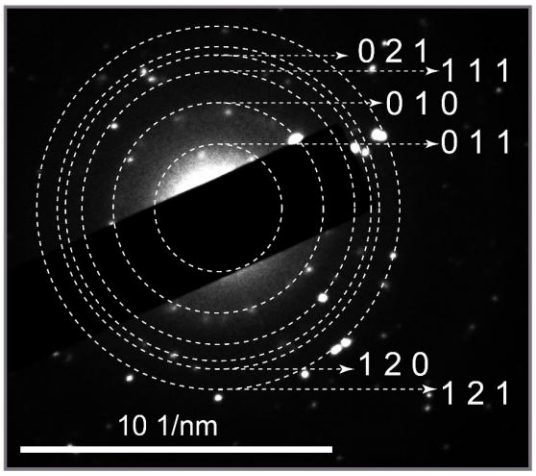

Supplementary Fig. 4. SAED pattern of core-shell DSNPs.

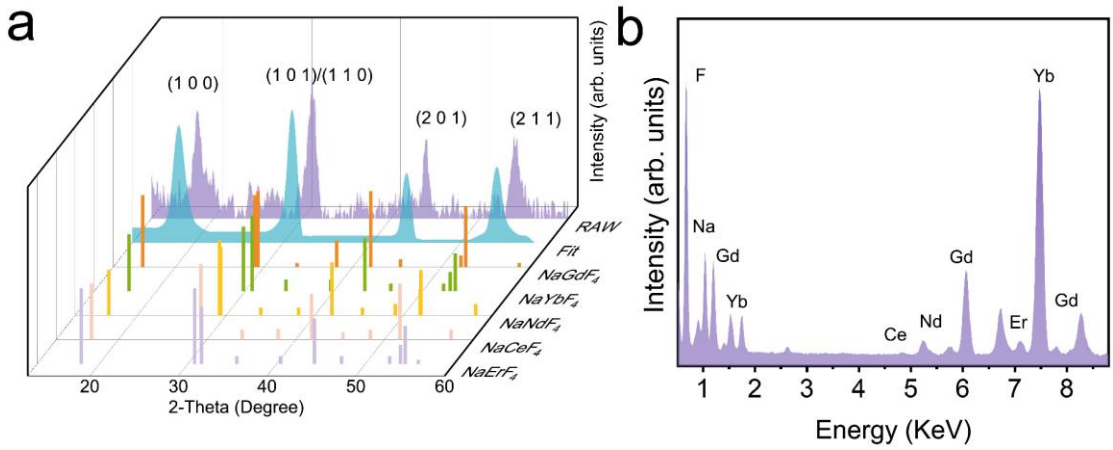

Supplementary Fig. 5. Crystal phase and elemental analysis of core-shell DSNPs. XRD pattern analysis (a) and EDS spectra (b) of $NaGdF_4$:Yb,Er,Ce@$NaGdF_4$:Yb,Nd. Source data are provided as a Source Data file.

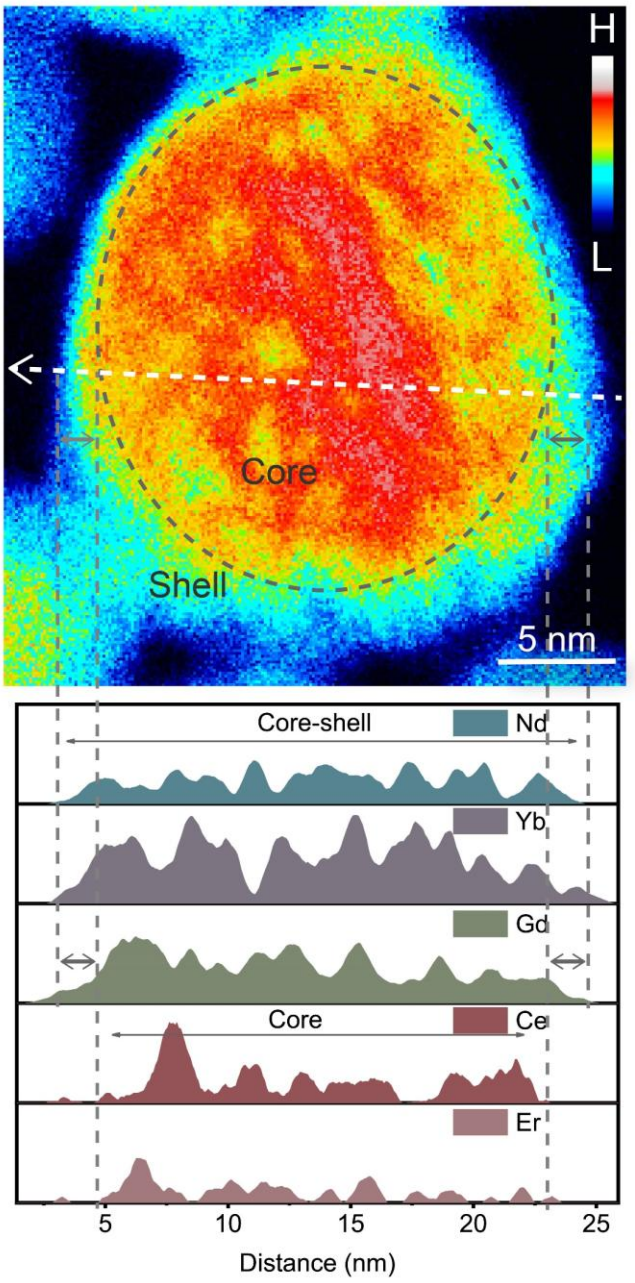

Supplementary Fig. 6. Elemental distribution analysis of core-shell lanthanide DSNPs. Aberration-corrected STEM-EDS line scan profile of a single $NaGdF_4$:Yb,Er,Ce@$NaGdF_4$:Yb,Nd nanoparticle. Source data are provided as a Source Data file.

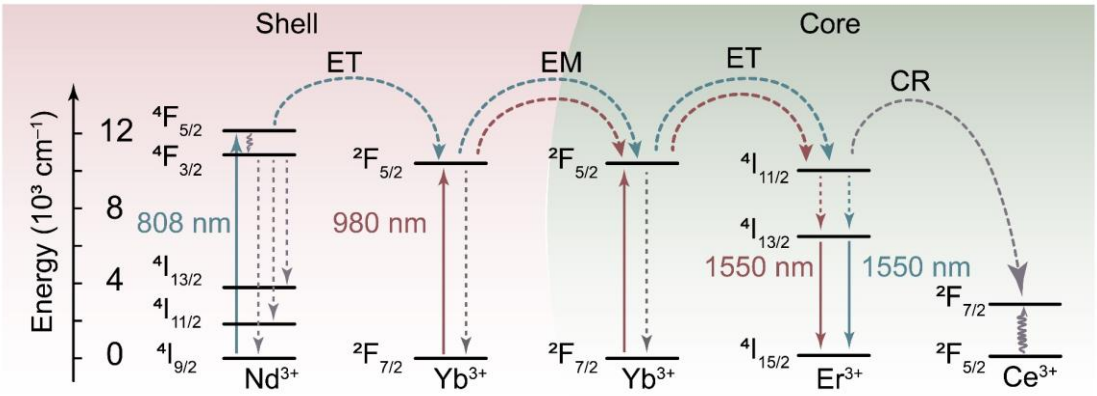

Supplementary Fig. 7. Schematic illustration of the simplified energy level diagram depicting the energy transfer of DSNPs under 808 nm and 980 nm excitation. ET, Energy transfer between lanthanide ions within the same shell layer; EM, energy migration from Yb^{3+} ions in the shell to Yb^{3+} ions located in the core; CR, non-radiative, phonon-assisted cross-relaxation between lanthanide ions.

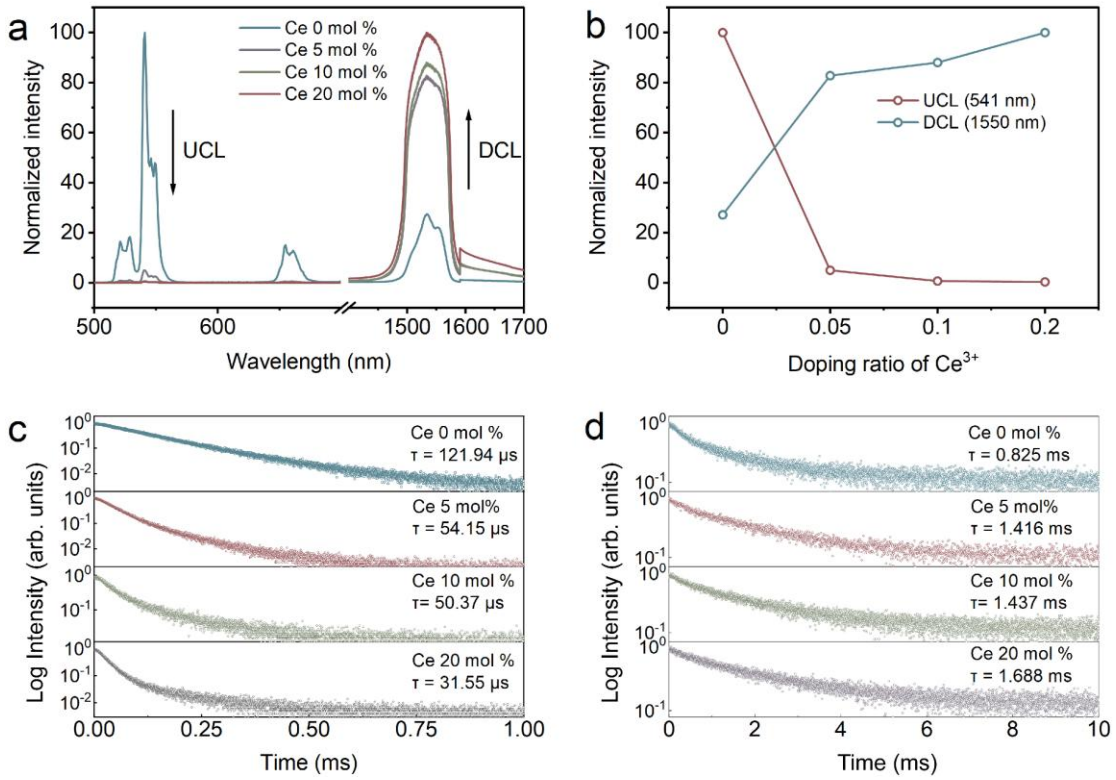

Supplementary Fig. 8. Characterization of the upconversion luminescence (UCL) and downconversion luminescence (DCL) properties of DSNPs with varying Ce^{3+} doping concentrations. (a) UCL and DCL emission spectra of DSNPs at different Ce^{3+} doping levels. (b) Quantitative analysis of the 541 nm UCL peak and the 1550 nm DCL peak intensities as a function of Ce^{3+} doping concentration. (c) Time-resolved fluorescence decay profiles monitored at 541 nm for DSNPs with varying Ce^{3+} doping under 980 nm excitation. (d) Time-resolved fluorescence decay profiles monitored at 1550 nm for DSNPs with varying Ce^{3+} doping under 980 nm excitation. Source data are provided as a Source Data file.

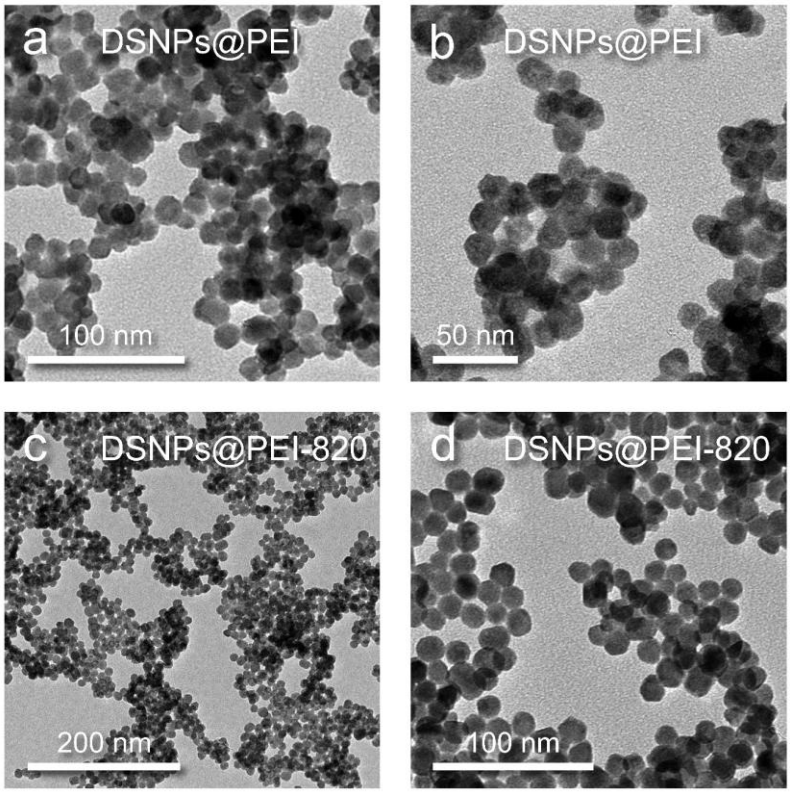

Supplementary Fig. 9. TEM images of lanthanide nanocomposites. TEM images of DSNPs@PEI (a and b) and DSNPs@PEI-820 (c and d).

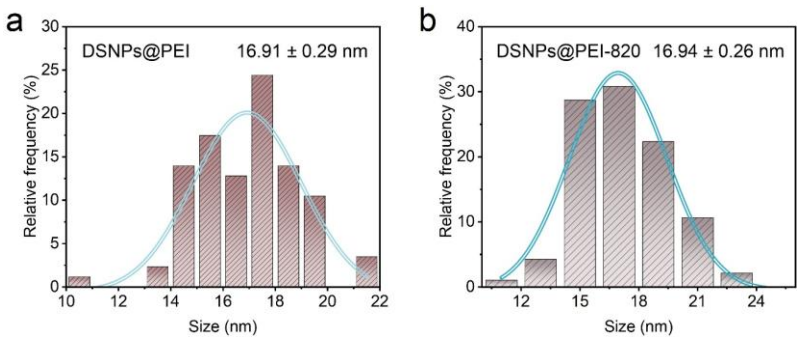

Supplementary Fig. 10. Particle size analysis of lanthanide nanocomposites. Particle size distribution of DSNPs@PEI (a) and DSNPs@PEI-820 (b). Source data are provided as a Source Data file.

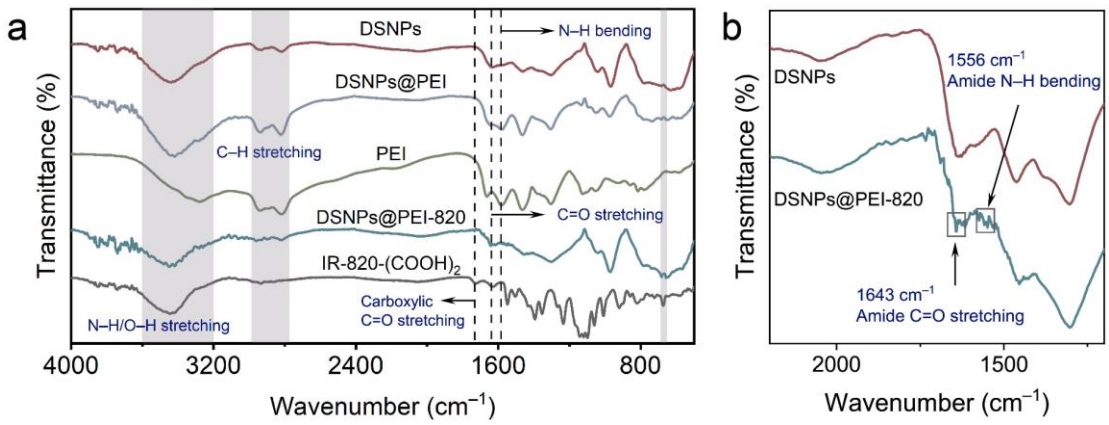

Supplementary Fig. 11. FT-IR characterization of lanthanide nanomaterials. (a) FT-IR profiles of IR-820-$(COOH)_2$, PEI, DSNPs, DSNPs@PEI, and DSNPs@PEI-820. (b) Magnified spectra of DSNPs and DSNPs@PEI-820 in the 1200-2200 cm^{-1} region. Source data are provided as a Source Data file.

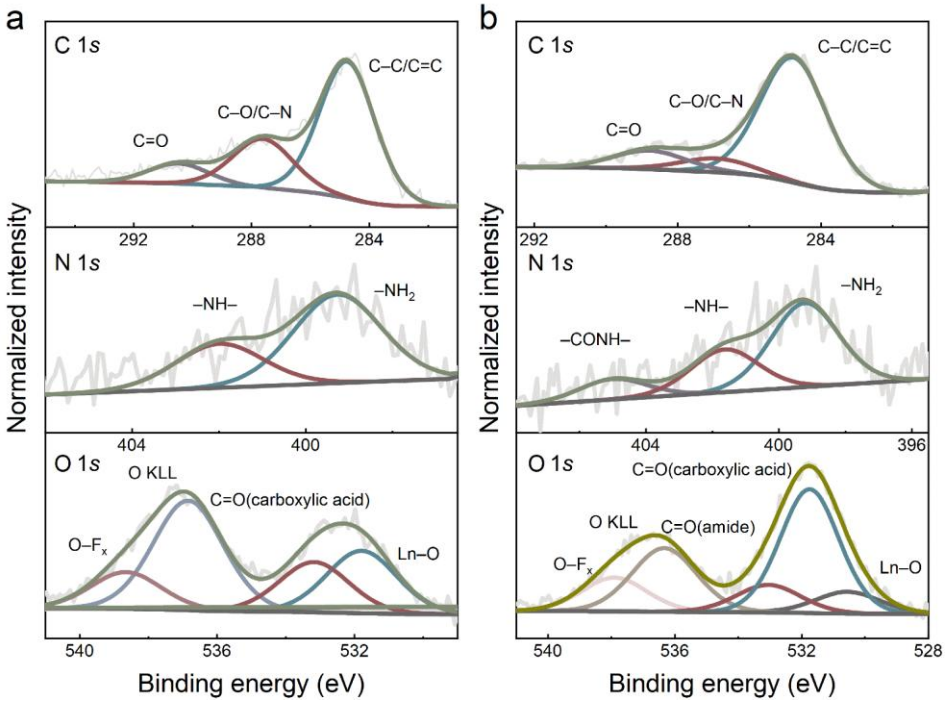

Supplementary Fig. 12. XPS Characterization of DSNPs@PEI and DSNPs@PEI-820. (a) High-resolution XPS spectra of C 1*s*, N 1*s*, and O 1*s* for DSNPs@PEI. (b) High-resolution XPS spectra of C 1*s*, N 1*s*, and O 1*s* for DSNPs@PEI-820. Source data are provided as a Source Data file.

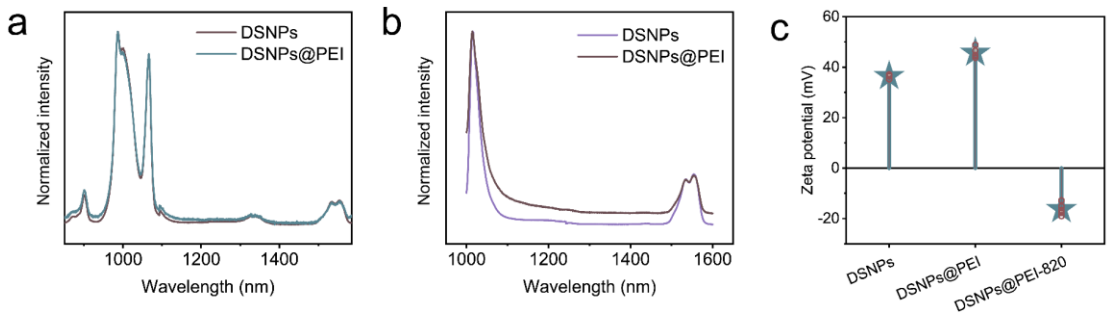

Supplementary Fig. 13. Characterization of emission properties and zeta potential of lanthanide nanomaterials. NIR-II region emission spectra of DSNPs and DSNPs@PEI under 808 nm (a) and 980 nm (b) laser excitation. (c) Zeta potential measurements of DSNPs, DSNPs@PEI, and DSNPs@PEI-820. The data are presented as mean ± SD (n = 5 independent samples). Source data are provided as a Source Data file.

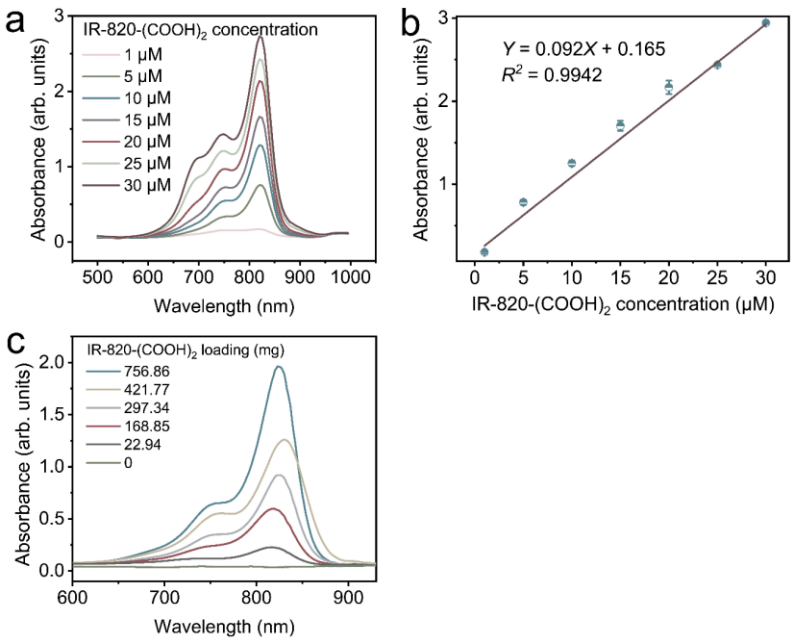

Supplementary Fig. 14. Determination of IR-820-$(COOH)_2$ loading of DSNPs@PEI-820. Absorption spectra (a) and concentration-absorbance calibration curves (b) for IR-820-$(COOH)_2$. Data are presented as mean ± SD (n = 5 independent samples). (c) Absorption spectra of DSNPs@PEI-820 with different loadings of IR-820-$(COOH)_2$. Source data are provided as a Source Data file.

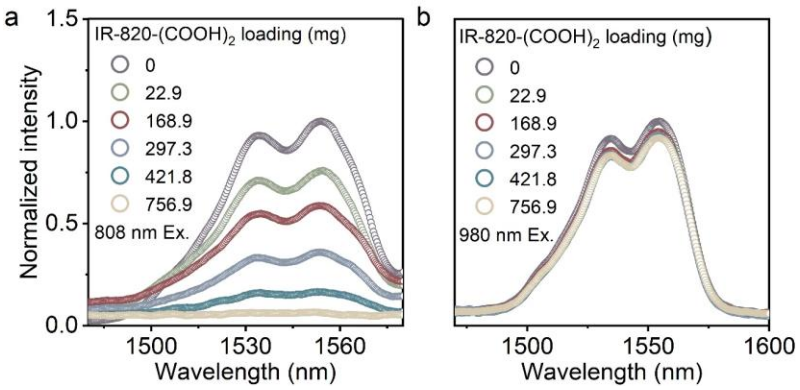

Supplementary Fig. 15. Emission characteristics of DSNPs@PEI-820 with different IR-820-$(COOH)_2$ loadings. Emission spectra of DSNPs@PEI-820 with different loadings of IR-820-$(COOH)_2$ (expressed as mass per mole of DSNPs) near 1550 nm, under excitation from 808 nm (a) and 980 nm (b) lasers. Source data are provided as a Source Data file.

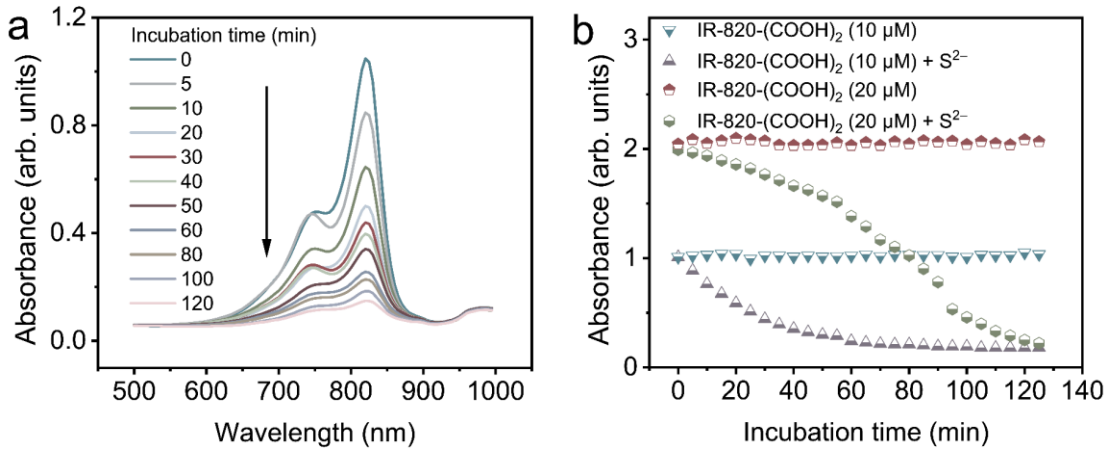

Supplementary Fig. 16. Evaluation of the response characteristics of IR-820-$(COOH)_2$ to H_2S. (a) Absorption spectra of IR-820-$(COOH)_2$-S^{2-} reaction system at different reaction times. (b) Absorbance versus incubation time curves for the IR-820-$(COOH)_2$-S^{2-} reaction system. The concentration of S^{2-} used in the reaction was 100 μM. Source data are provided as a Source Data file.

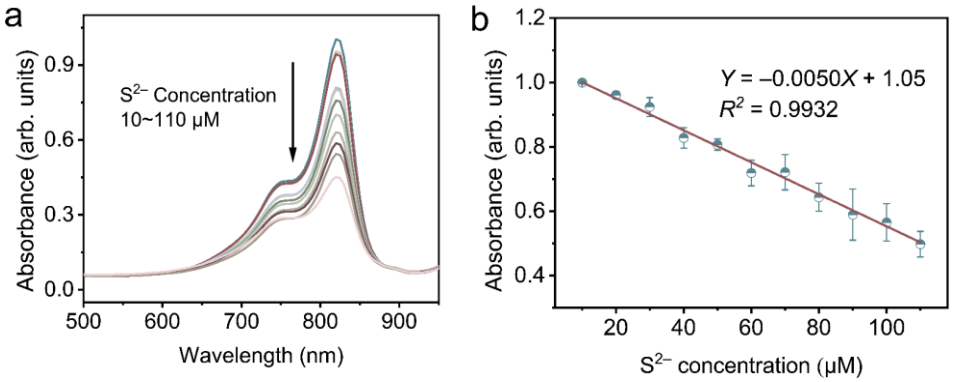

Supplementary Fig. 17. Quantitative evaluation of the H_2S response characteristics of IR-820-$(COOH)_2$. (a) Absorption spectra and (b) calibration curves of S^{2-} concentration versus absorbance for the IR-820-$(COOH)_2$-S^{2-} reaction system. Data are presented as mean ± SD (n = 5 independent samples). Source data are provided as a Source Data file.

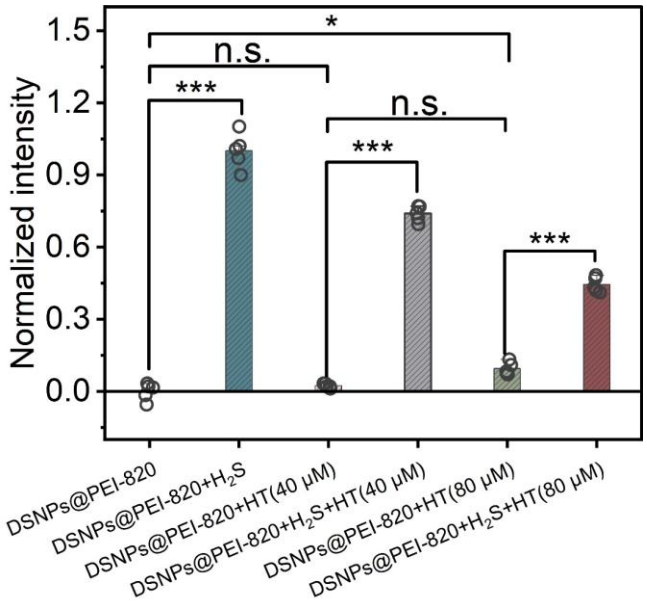

Supplementary Fig. 18. Target selectivity evaluation of DSNPs@PEI-820 via H_2S scavenging assay. Inhibitory effect of the H_2S scavenger hypotaurine (HT) on the response intensity of DSNPs@PEI-820 under 808 nm laser excitation. Data are presented as mean ± SD (n = 5 independent samples). Statistical analysis was performed using one-way ANOVA followed by Tukey's multiple comparison test to evaluate intergroup differences (*P < 0.05, **P < 0.01, ***P < 0.001). Source data are provided as a Source Data file.

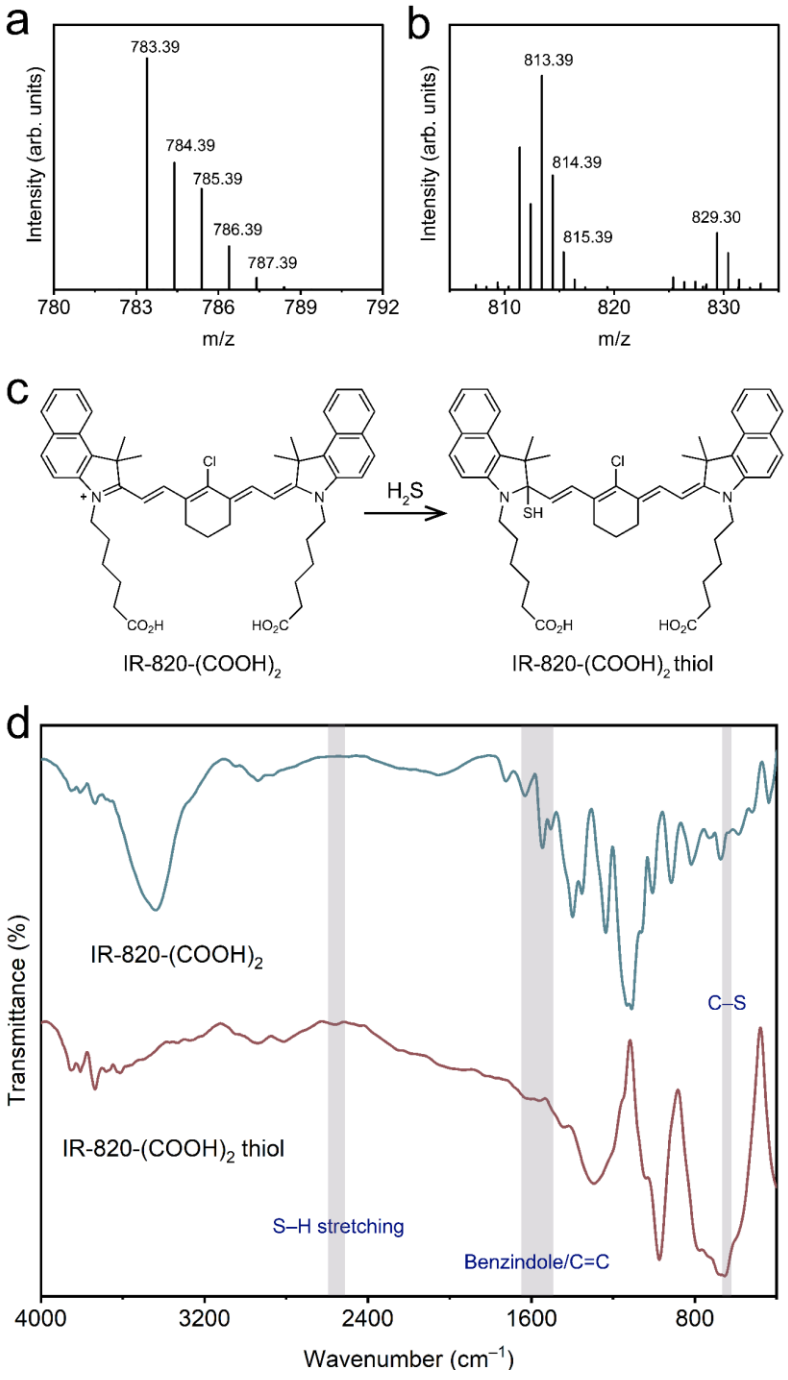

Supplementary Fig. 19. Mechanistic study of the nucleophilic addition reaction between IR-820-(COOH)$_2$ and H_2S. HRMS analysis of IR-820-(COOH)$_2$ (a) and IR-820-(COOH)$_2$ thiol (b). (c) Schematic diagram of the reaction mechanism of IR-820-(COOH)$_2$ with S^{2-}. (d) FT-IR profiles of both IR-820-(COOH)$_2$ and IR-820-(COOH)$_2$ thiol. Source data are provided as a Source Data file.

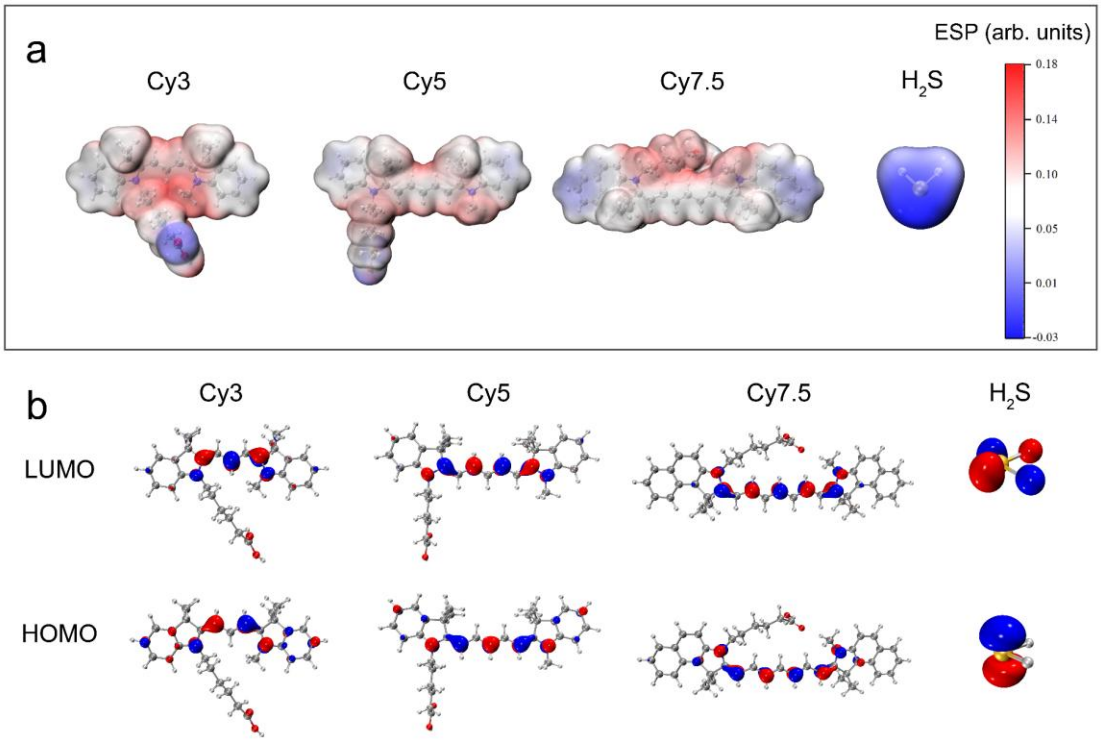

Supplementary Fig. 20. DFT study on cyanine dyes and H_2S reaction mechanism. (a) Electrostatic potential surface maps of Cy3, Cy5, Cy7.5, and H_2S. (b) Frontier orbital characteristics of Cy3, Cy5, Cy7.5 and H_2S.

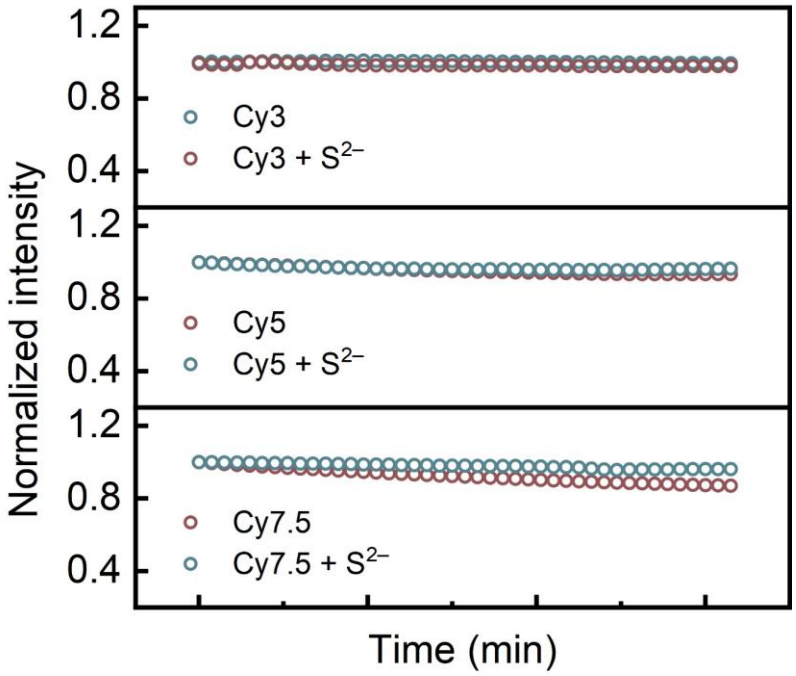

Supplementary Fig. 21. Evaluation of nucleophilic addition reactivity between cyanine dyes and H_2S. Time-dependent absorbance changes of Cy3, Cy5, and Cy7.5 during co-incubation with S^{2-}. Source data are provided as a Source Data file.

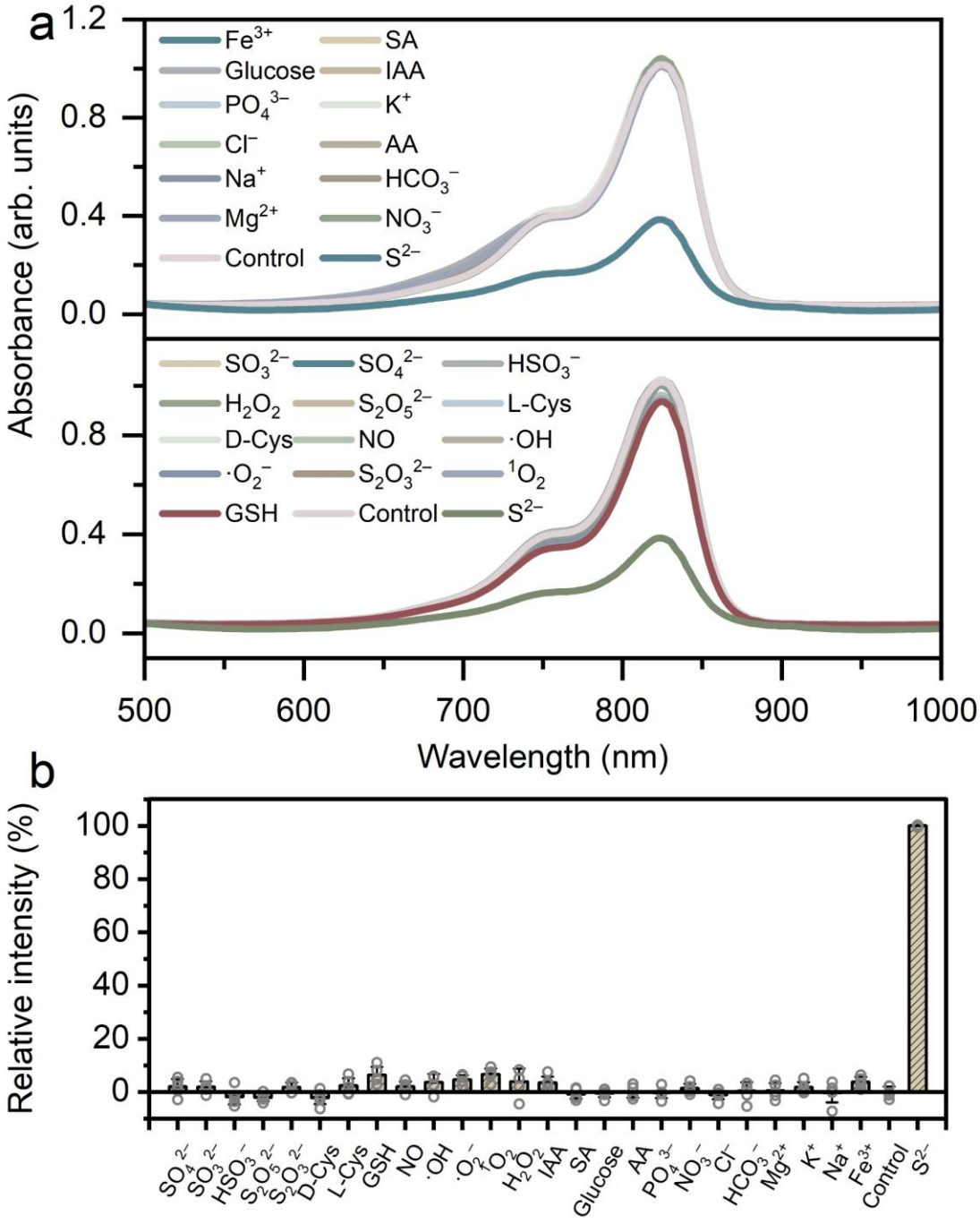

Supplementary Fig. 22. Reaction selectivity test of IR-820-$(COOH)_2$ to S^{2-}. (a) Absorption spectra of the IR-820-$(COOH)_2$-S^{2-} reaction system following the addition of different plant endogenous interferents. (b) Analysis of the interference intensity in the IR-820-$(COOH)_2$-S^{2-} reaction system caused by different plant endogenous interferents. The selectivity experiments were conducted in a 20 mM MES buffer solution at pH 5.5. Data are presented as mean ± SD (n = 5 independent samples). Source data are provided as a Source Data file.

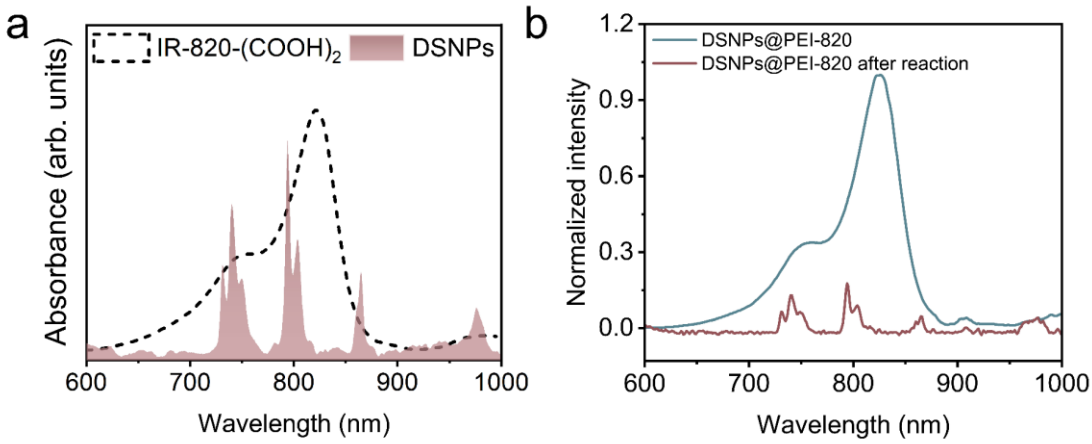

Supplementary Fig. 23. Absorption spectroscopic analysis of IR-820-$(COOH)_2$, DSNPs, and DSNPs@PEI-820 before and after reaction with S^{2-}. (a) UV-Vis absorption spectra of IR-820-$(COOH)_2$ and DSNPs in the wavelength range of 600–1000 nm. (b) Absorption spectra of DSNPs@PEI-820 before and after reaction with S^{2-}. Source data are provided as a Source Data file.

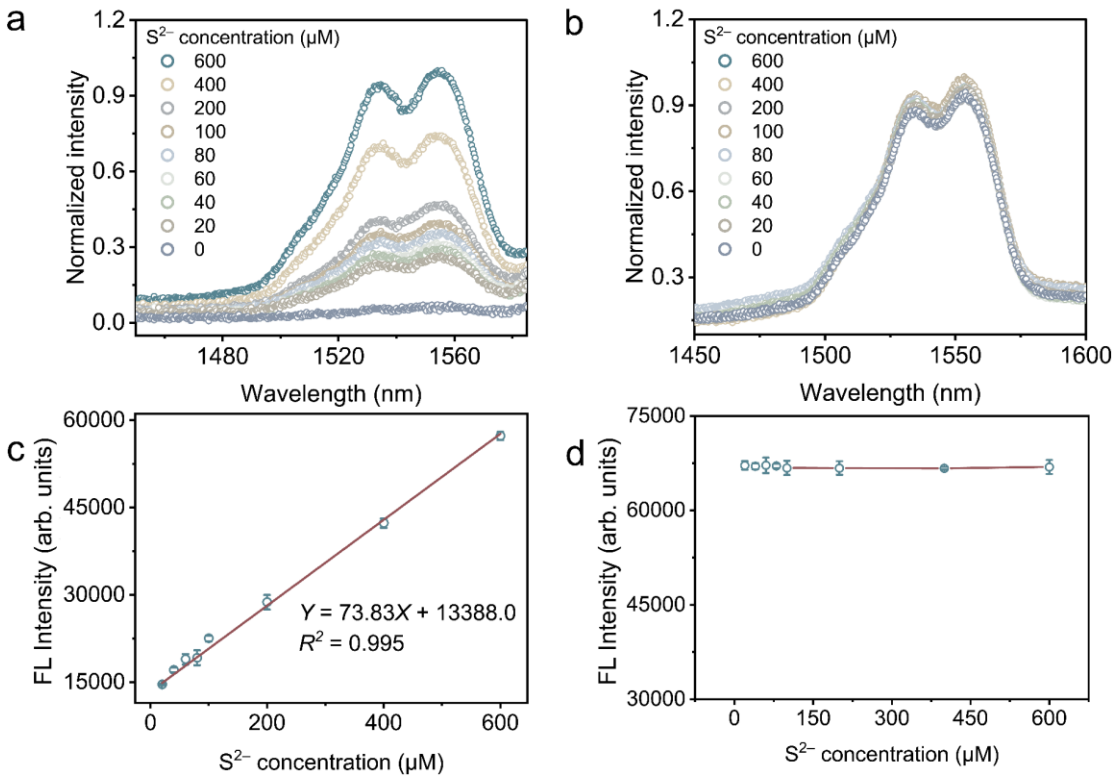

Supplementary Fig. 24. Quantification of the response of DSNPs@PEI-820 to S^{2-}. NIR-II spectra of S^{2-} concentration versus DSNPs@PEI-820 fluorescence intensity under 808 nm (a) and 980 nm (b) laser excitation. Fluorescence intensities were normalized to the intensity at 1550 nm obtained in the presence of 600 μM S^{2-}. Corresponding calibration curves of S^{2-} concentration versus DSNPs@PEI-820 fluorescence intensity at 1550 nm under 808 nm (c) and 980 nm (d) laser excitation. Data are presented as mean ± SD (n = 5 independent samples). Source data are provided as a Source Data file.

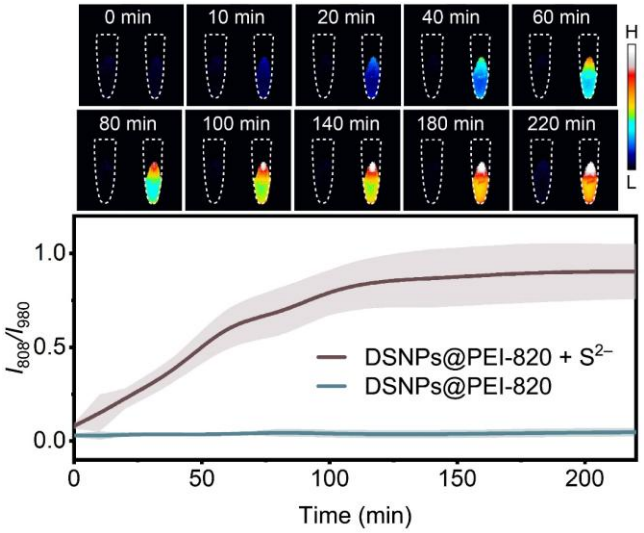

Supplementary Fig 25. Time-dependent fluorescence response of DSNPs@PEI-820 to S^{2-}. In the fluorescence images at each time point, the centrifuge tubes on the left and right correspond to the DSNPs@PEI-820 group and the DSNPs@PEI-820 + S^{2-} group, respectively. Data are presented as mean ± SD (n = 5 independent samples), with shaded regions indicating the SD of the ratiometric signal intensity. Source data are provided as a Source Data file.

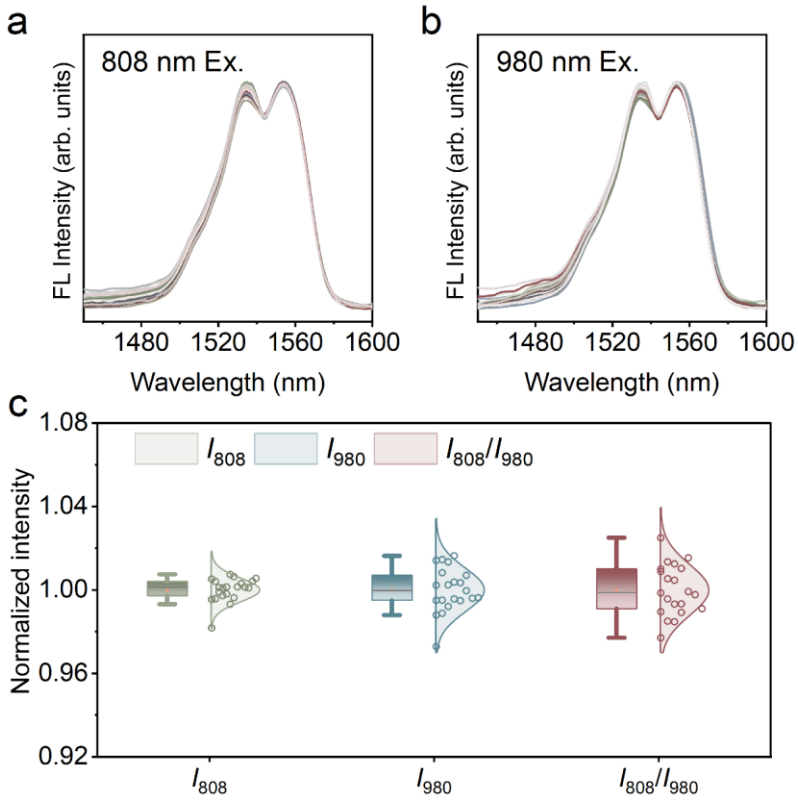

Supplementary Fig 26. Stability test of DSNPs@PEI-820 in response to S^{2-}. Emission spectra of DSNPs@PEI-820 in response to S^{2-} across multiple replicate experiments (n = 21 independent samples, measured on different days under identical conditions) with 808 nm (a) and 980 nm (b) laser excitation, along with the corresponding fluorescence intensity statistics (c). Source data are provided as a Source Data file.

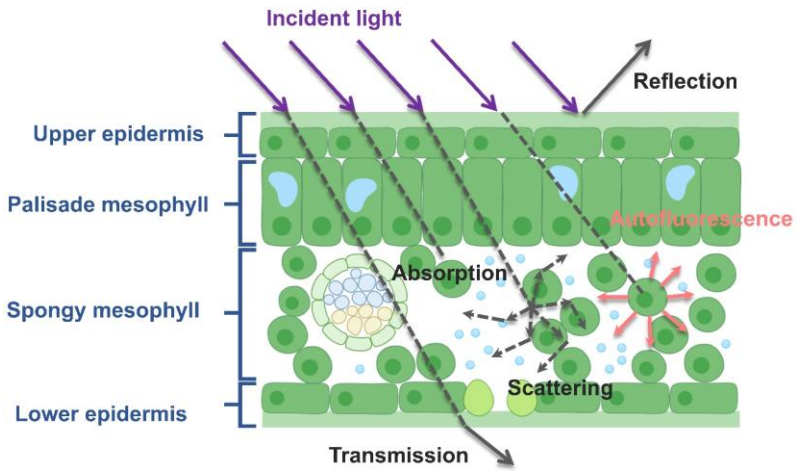

Supplementary Fig. 27. Schematic illustration of complex photon-tissue interactions within plant leaf tissue[33–35]**.** The leaf cross-section framework was created in BioRender. Wang, Y. (2026) https://BioRender.com/k6p4ks5.

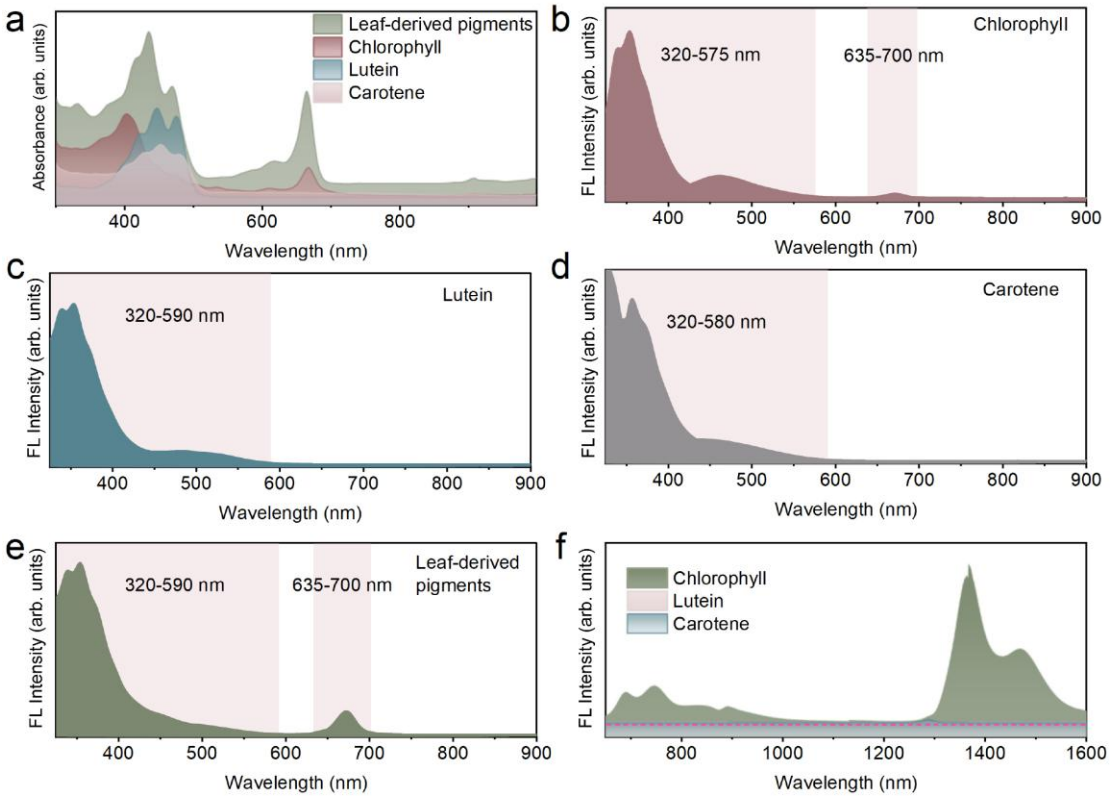

Supplementary Fig. 28. Autofluorescence assessment of the main fluorescent pigments in lettuce leaves in the UV-Vis and NIR regions. UV-Vis absorption spectra (a) and fluorescence emission spectra of chlorophyll (b), lutein (c), carotene (d), and pigment mixtures extracted from leaves (e). The spectra in (b–e) were constructed by merging multiple emission curves acquired under various excitation wavelengths ranging from 280 to 635 nm. All pink shaded regions indicate the spectral windows where leaf autofluorescence may interfere with imaging. (f) NIR fluorescence spectra of chlorophyll, lutein, and carotene under 635 nm laser excitation. Source data are provided as a Source Data file.

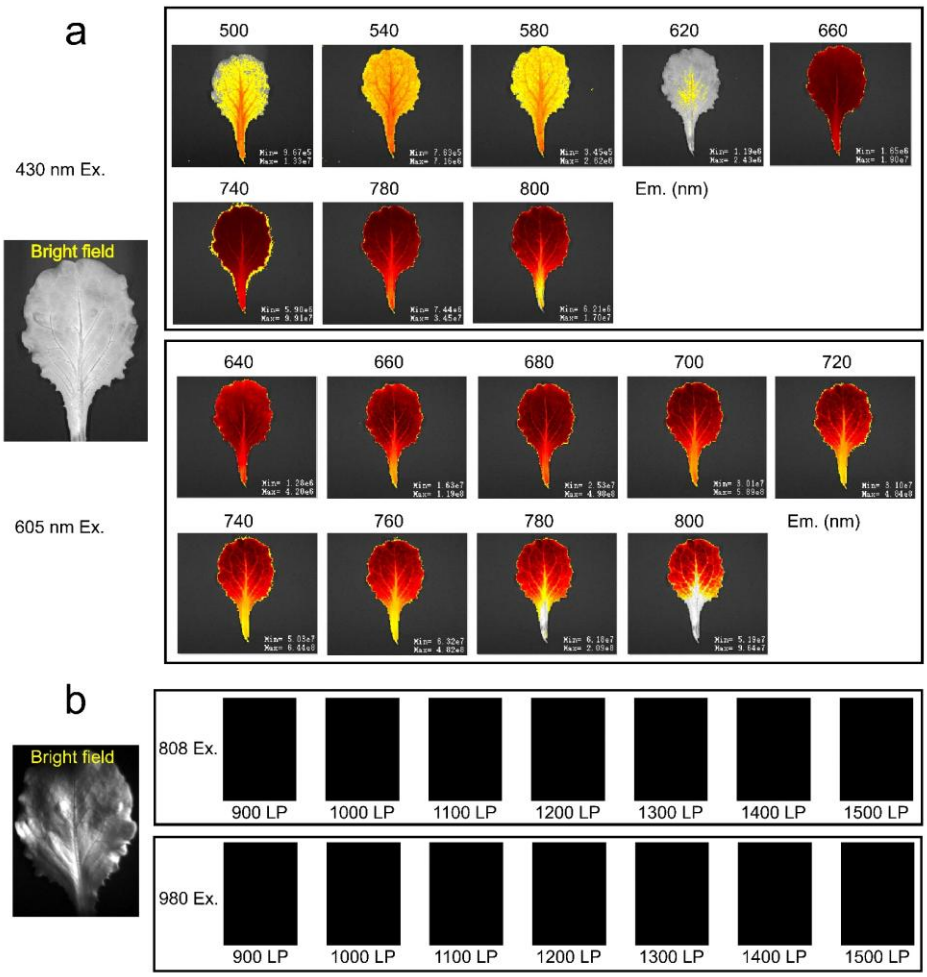

Supplementary Fig. 29. Imaging of autofluorescence of lettuce leaves at different excitation wavelengths. (a) Autofluorescence intensity of lettuce leaves recorded at different wavelengths under excitation from 430 nm and 605 nm light sources. (b) Autofluorescence intensity of lettuce leaves recorded in the NIR-II region under 808 nm and 980 nm laser excitation.

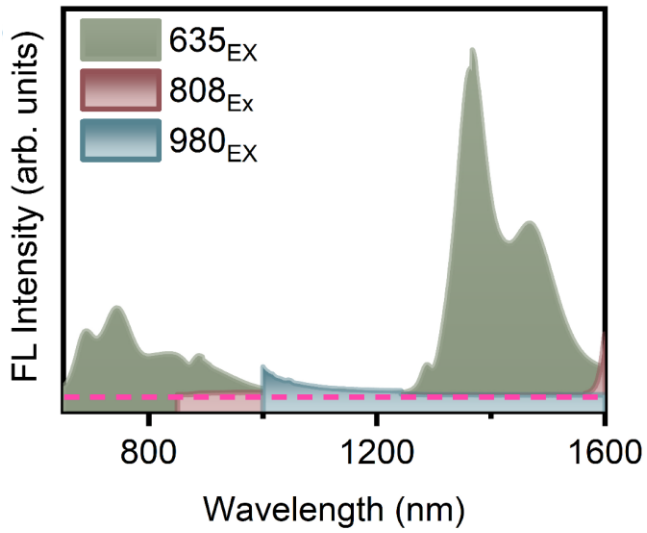

Supplementary Fig. 30. NIR autofluorescence assessment of chlorophyll under different excitation wavelengths. Fluorescence emission spectra of chlorophyll under 635 nm, 808 nm, and 980 nm laser excitation. Source data are provided as a Source Data file.

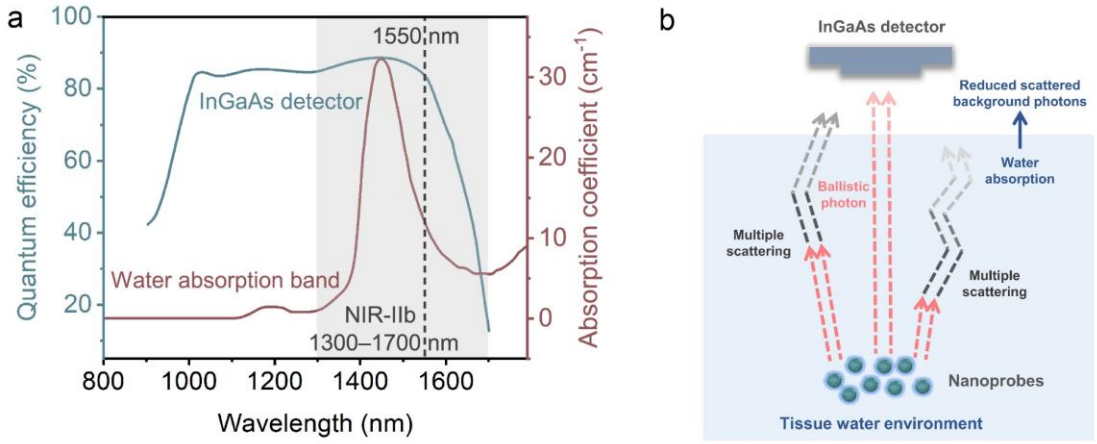

Supplementary Fig. 31. Mechanism of water absorption-mediated background suppression. (a) Wavelength-dependent quantum efficiency of the InGaAs detector and the absorption coefficient of water. The shaded regions indicate the water absorption bands within the NIR-IIb region. (b) Schematic illustration of the spatial filtering effect caused by tissue water, where multiply scattered photons with longer optical paths are preferentially attenuated[36,37]. Source data are provided as a Source Data file.

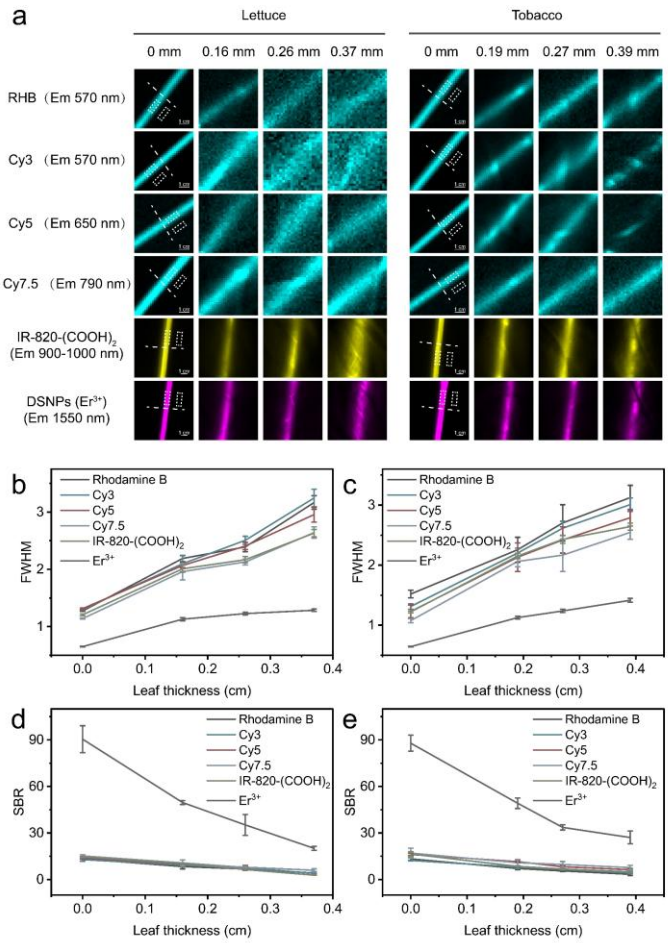

Supplementary Fig. 32. Evaluation of fluorescence imaging performance of visible, NIR-I, and NIR-IIb probes through lettuce and tobacco leaves of varying thicknesses. (a) Fluorescence images of Rhodamine B (RHB), Cy3, Cy5, Cy7.5, IR-820-$(COOH)_2$, and DSNPs@PEI in the visible/NIR-I/II windows, covered with lettuce and tobacco leaves of varying thicknesses. Representative images from five independent biological replicates are shown, with similar results obtained in all replicates. FWHM for the visible/NIR-I/II windows at different penetration depths through lettuce (b) and tobacco (c) leaves. FWHM was determined by calculating the fluorescence intensity along the white dashed lines in each group of panel (a). Data are presented as mean ± SD (n = 5 independent samples). SBR for the visible/NIR-I/II windows at different penetration depths through lettuce (d) and tobacco (e) leaves. SBR was determined by calculating the fluorescence intensity within the white box regions in each group of panel (a). Data are presented as mean ± SD (n = 5 independent samples). Source data are provided as a Source Data file.

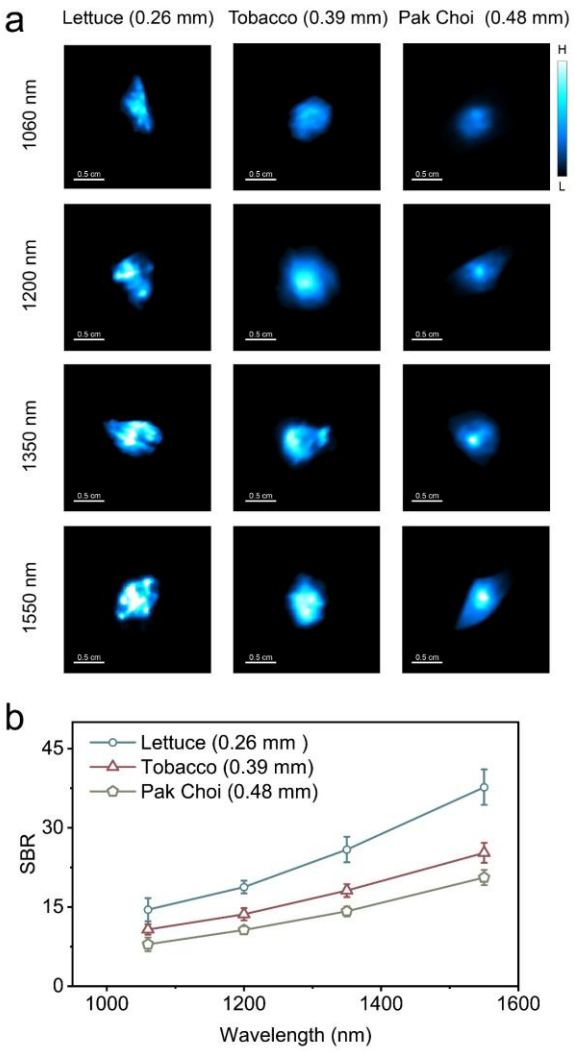

Supplementary Fig. 33. Comparative evaluation of *in vivo* imaging performance across different NIR-II emission wavelengths in plant leaves of varying thickness. (a) NIR-II fluorescence images of intact lettuce (0.26 mm), tobacco (0.39 mm), and pak choi (0.48 mm) leaves obtained using representative nanoprobes emitting at 1060 nm ($NaGdF_4$:Nd), 1200 nm (Ag_2S), 1350 nm ($NaGdF_4$:Nd), and 1550 nm (DSNPs). Representative images from five independent biological replicates are shown, with similar results obtained in all replicates. (b) Quantitative analysis of the SBR across various emission wavelengths for the three leaf types. Data are presented as mean ± SD (n = 5 independent samples). Prior to injection, the fluorescence intensities of the nanoprobe MES solutions were pre-calibrated to identical levels *in vitro* at their respective emission wavelengths. Source data are provided as a Source Data file.

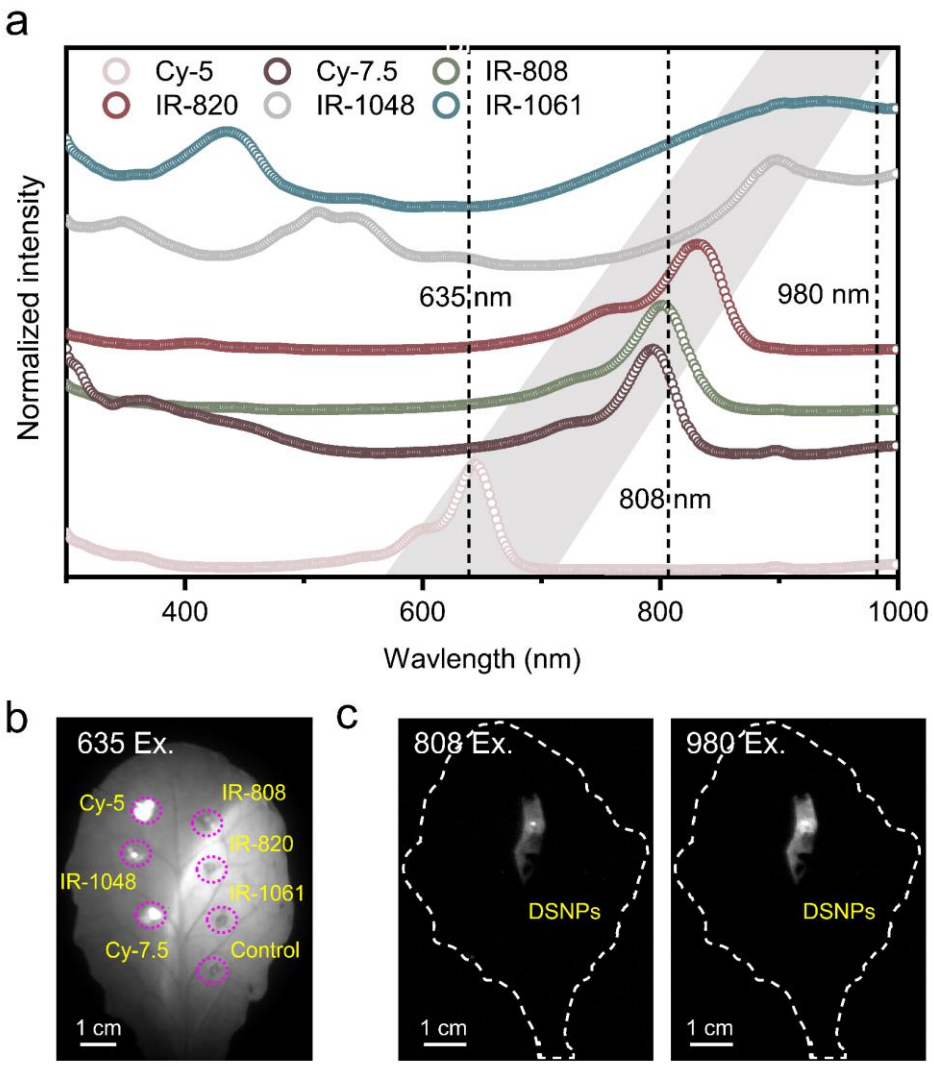

Supplementary Fig. 34. Advantage of DSNPs in leaf imaging free from autofluorescence interference. (a) Absorption spectra of common ICG-based fluorescent probes. (b) Fluorescence imaging of lettuce leaves infiltrated with ICG-based probes under 635 nm laser excitation, utilizing a 650 nm long-pass filter. The purple dashed circles indicate the probe injection sites. (c) Fluorescence imaging of lettuce leaves infiltrated with DSNPs under 808 nm and 980 nm laser excitation, utilizing a 1400 nm long-pass filter. Source data are provided as a Source Data file.

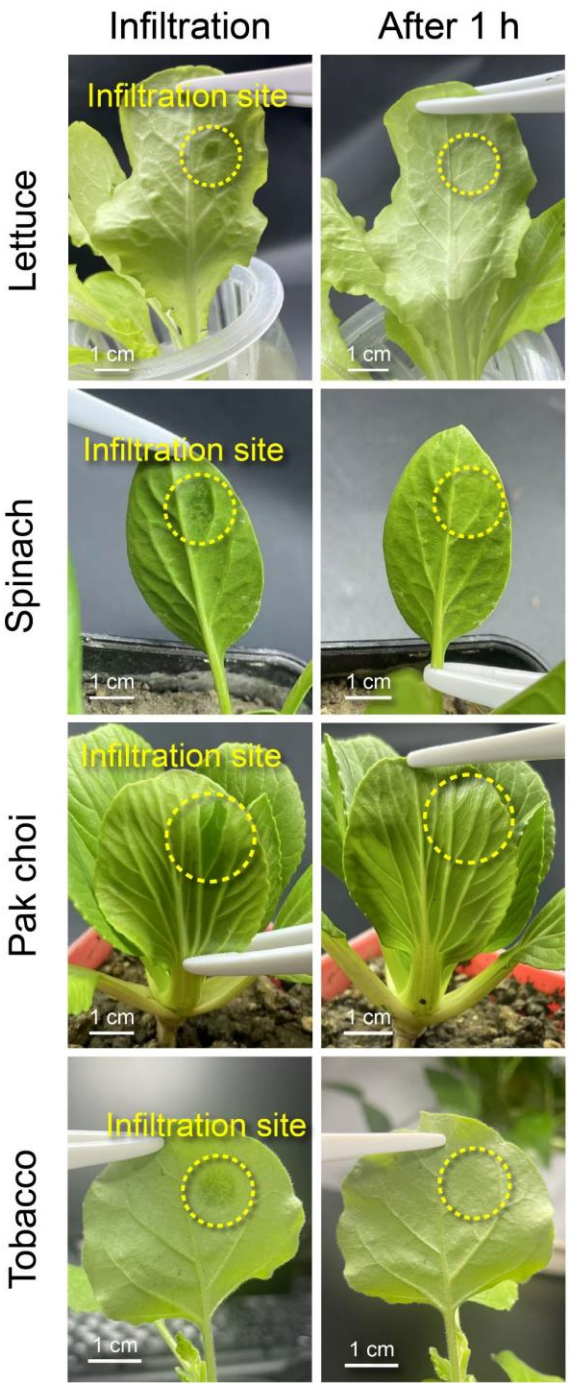

Supplementary Fig. 35. Optical photographs of DSNPs@PEI-820 infiltrating through the stomata of lettuce, spinach, pak choi, and tobacco leaves. Representative images from five independent biological replicates are shown, with similar results obtained in all replicates.

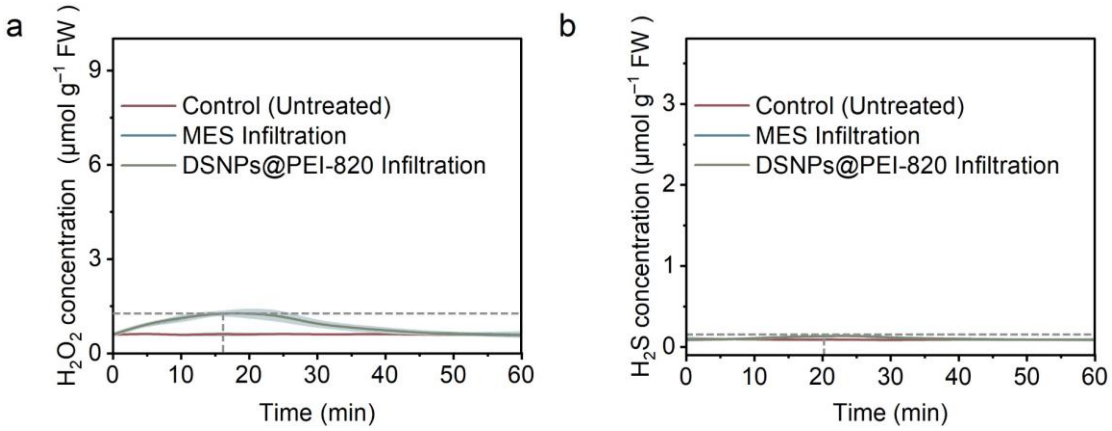

Supplementary Fig. 36. Evaluation of H_2O_2 and H_2S signals in lettuce leaves following needle-free injection of DSNPs@PEI-820, measured by colorimetric assays. (a) Evaluation of H_2O_2 oxidative signals in lettuce leaves following needle-free injection of DSNPs@PEI-820. Data are presented as mean ± SD (n = 5 independent samples), with shaded regions indicating the SD of the measured concentration. (b) Evaluation of H_2S signals in lettuce leaves following needle-free injection of DSNPs@PEI-820. Data are presented as mean ± SD (n = 5 independent samples), with shaded regions indicating the SD of the measured concentration[38,39]. Source data are provided as a Source Data file.

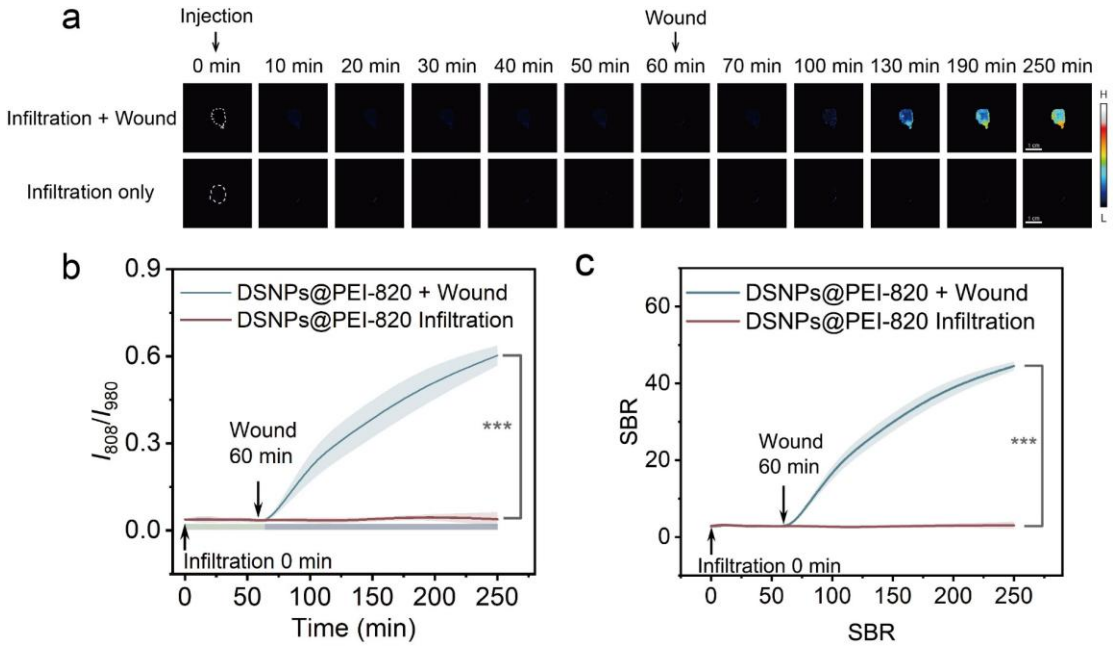

Supplementary Fig. 37. *In situ* monitoring of endogenous H_2S fluctuations using DSNPs@PEI-820 following needle-free infiltration. (a) Time-dependent NIR-II fluorescence imaging of plant leaves subjected to needle-free infiltration only or followed by wound stress. Representative images from five independent biological replicates are shown, with similar results obtained in all replicates. (b) Quantitative temporal profiles of the ratiometric fluorescence intensity. Data are presented as mean ± SD (n = 5 independent samples), with shaded regions indicating the SD of the ratiometric signal intensity. Statistical analysis was performed using one-way ANOVA followed by Tukey's multiple comparison test to evaluate intergroup differences (*P < 0.05, **P < 0.01, ***P < 0.001). (c) Corresponding dynamic changes in the SBR. Data are presented as mean ± SD (n = 5 independent samples), with shaded regions indicating the SD of the SBR. Statistical analysis was performed using one-way ANOVA followed by Tukey's multiple comparison test to evaluate intergroup differences (*P < 0.05, **P < 0.01, ***P < 0.001). Source data are provided as a Source Data file.

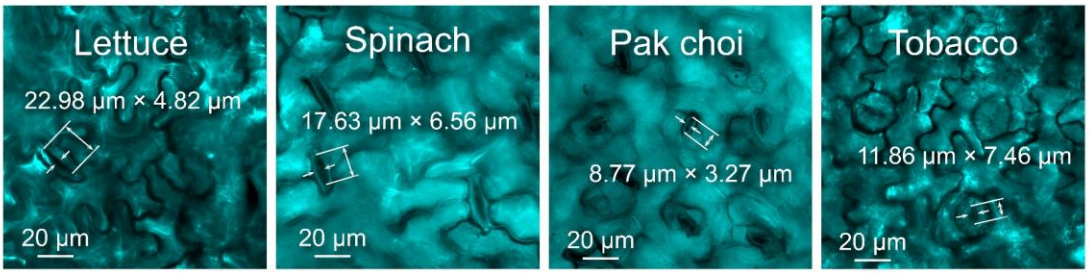

Supplementary Fig. 38. Optical micrographs of stomata in the lower epidermis of lettuce, spinach, pak choi, and tobacco leaves. Representative images from five independent biological replicates are shown, with similar results obtained in all replicates.

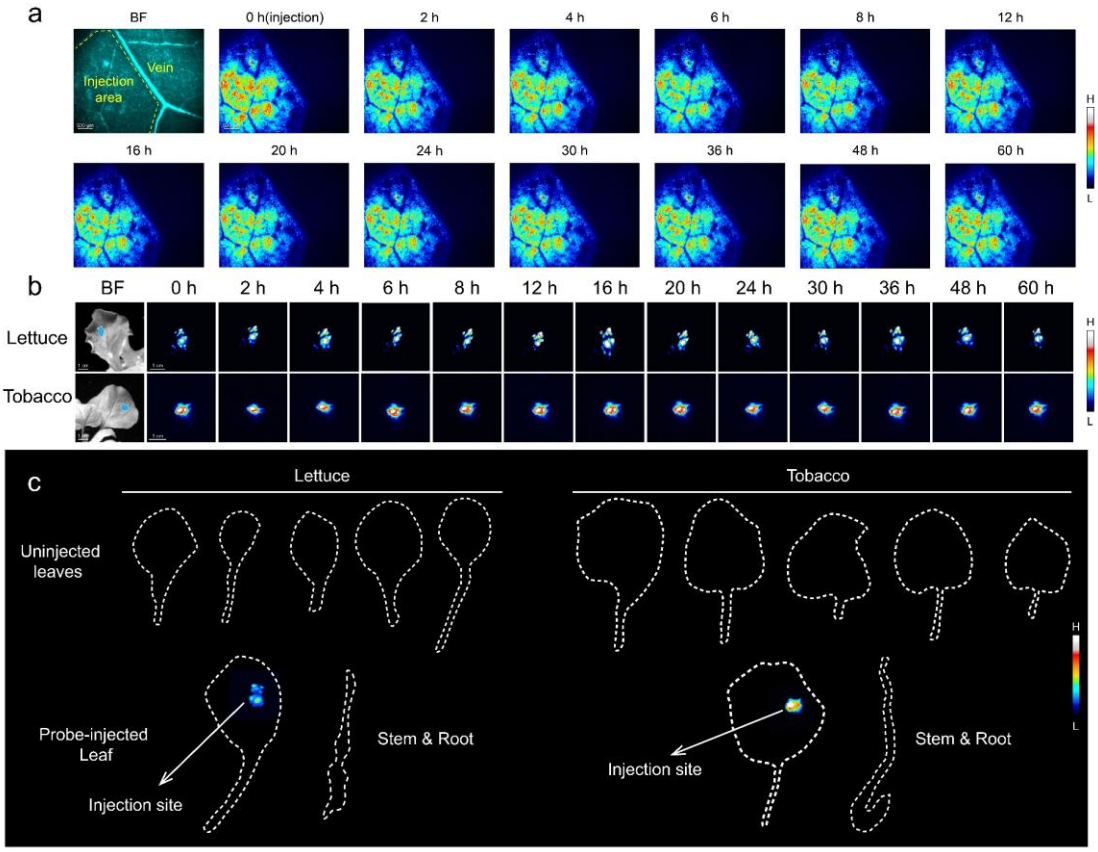

Supplementary Fig. 39. Spatiotemporal distribution, structural confinement, and long-term retention of DSNPs@PEI-820 following needle-free leaf injection. (a) Microscopic fluorescence images of the injection site at 60 h post-injection. (b) Continuous macroscopic NIR-IIb fluorescence imaging of lettuce and tobacco leaves over a 60-h period post-injection. (c) Fluorescence images illustrating the spatial distribution of the nanoprobe across different plant organs at 60 h post-infiltration. Representative images from five independent biological replicates are shown, with similar results obtained in all replicates.

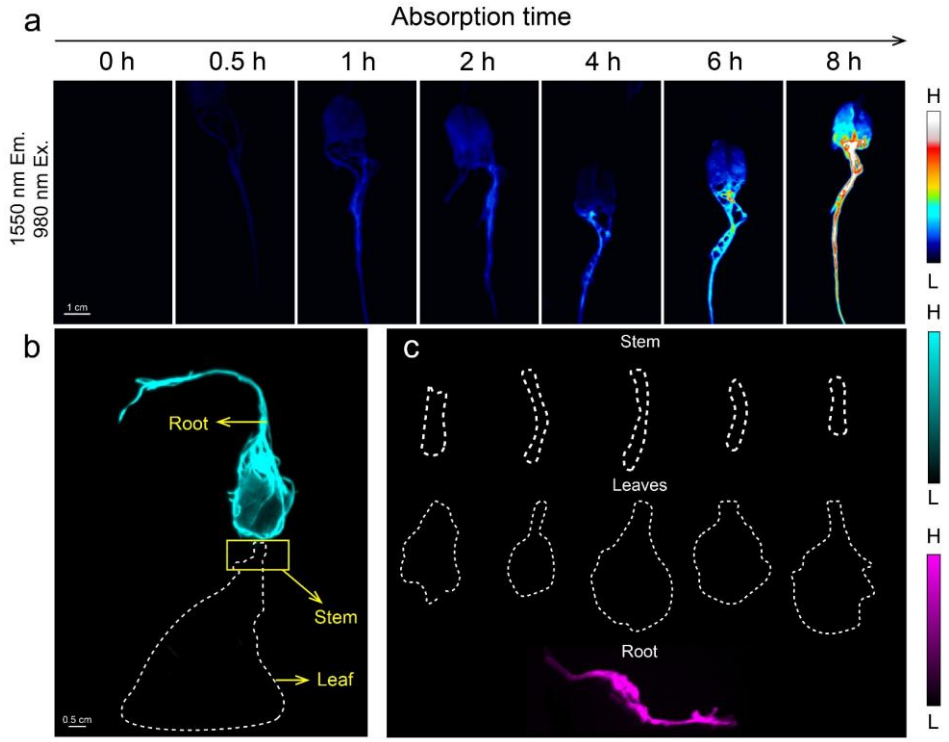

Supplementary Fig. 40. Evaluation of root absorption dynamics and systemic transport limitations of DSNPs@PEI-820 in hydroponically grown lettuce. (a) Time-dependent macroscopic NIR-IIb fluorescence images of lettuce roots immersed in a DSNPs@PEI-820 MES solution. (b) NIR-IIb fluorescence imaging of various plant tissues following the root absorption period. (c) NIR-IIb fluorescence images illustrating the spatial distribution of the nanoprobe across separated plant organs after the root absorption period. Representative images from five independent biological replicates are shown, with similar results obtained in all replicates.

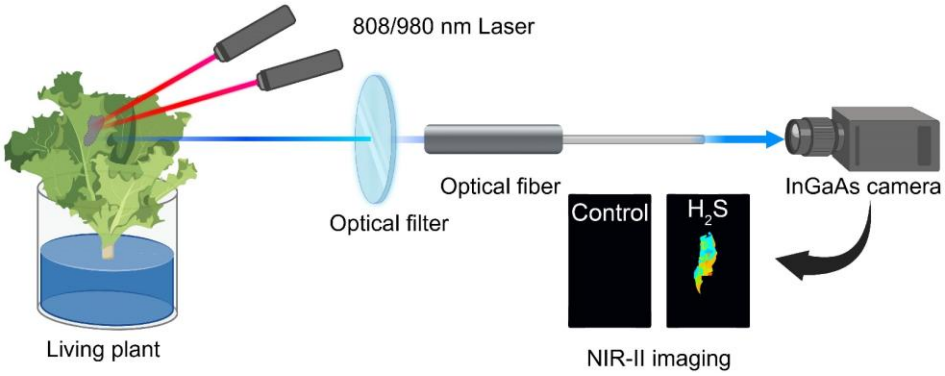

Supplementary Fig. 41. Schematic illustration of the ratiometric NIR imaging principle for the *in situ* detection of H_2S using DSNPs@PEI-820. The schematic frameworks and major elements of the imaging principles were created in BioRender. Feng, J. (2026) https://BioRender.com/141w3fj.

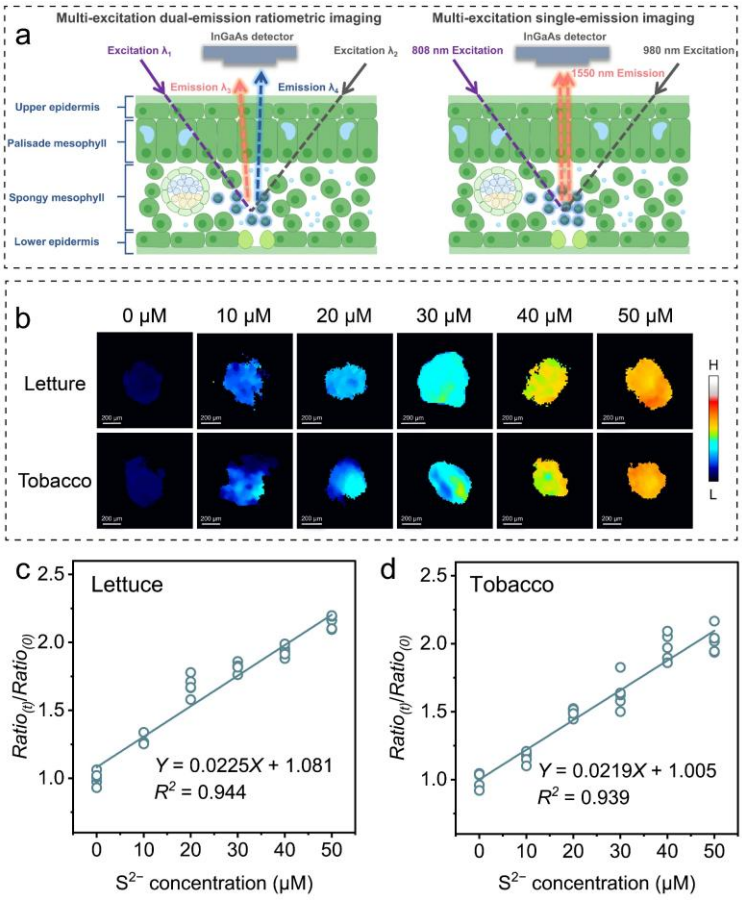

Supplementary Fig. 42. Dual-excitation/single-emission optical design and *in vivo* ratiometric calibration of DSNPs@PEI-820 for H_2S quantification in different plant tissues. (a) Schematic illustration of the dual-excitation (808 nm and 980 nm) and single-emission (1550 nm) optical paths within the anatomical layers of a plant leaf. The leaf cross-section framework was created in BioRender. Wang, Y. (2026) https://BioRender.com/k6p4ks5. (b) Representative *in vivo* NIR-II ratiometric fluorescence images of DSNPs@PEI-820 in lettuce and tobacco leaves infiltrated with exogenous H_2S across a concentration gradient. Representative images from five independent biological replicates are shown, with similar results obtained in all replicates. (c, d) Linear correlation between the ratiometric fluorescence signals and exogenous H_2S concentrations established within the leaf tissues of (c) lettuce and (d) tobacco. $Ratio_{(t)}/Ratio_{(0)}$ denotes the ratio of the ratiometric fluorescence intensity after *(t)* and before *(0)* the nanoprobe's response to H_2S. Data are presented as mean ± SD (n = 5 independent samples). Source data are provided as a Source Data file.

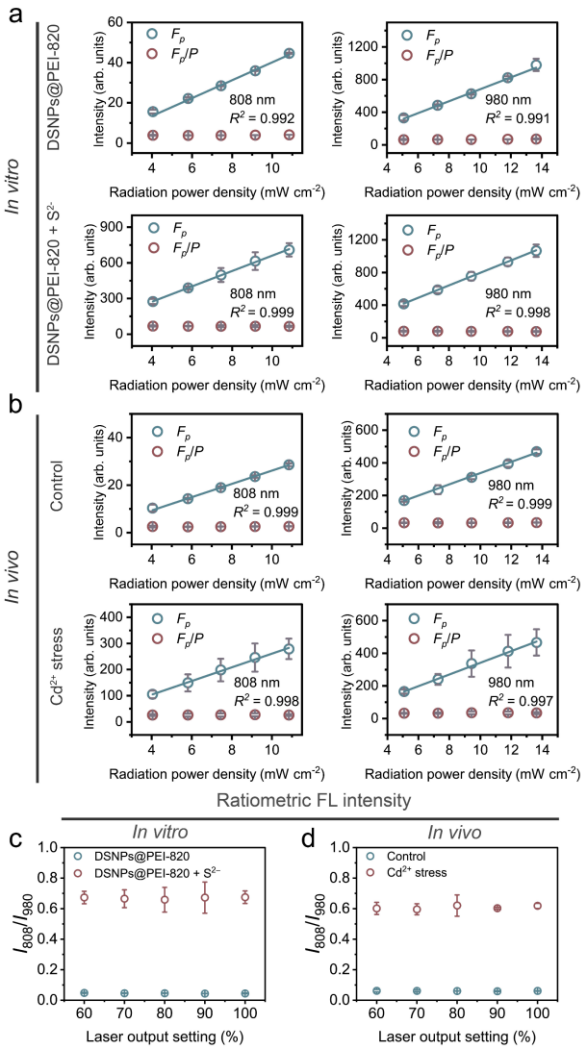

Supplementary Fig. 43. Evaluation of the photophysical stability and ratiometric robustness of the nanoprobe under varying excitation power densities. (a) Dependence of the absolute fluorescence intensity (F_p) and the power-normalized intensity (F_p/P) on the radiation power density for DSNPs@PEI-820 *in vitro* under 808 nm and 980 nm excitation. Data are presented as mean ± SD (n = 5 independent samples). (b) Dependence of the absolute fluorescence intensity and power-normalized intensity on the radiation power density for DSNPs@PEI-820 *in vivo* under 808 nm and 980 nm excitation. Data are presented as mean ± SD (n = 5 independent samples). (c) Ratiometric fluorescence signals of DSNPs@PEI-820 *in vitro* recorded at varying laser output settings. Data are presented as mean ± SD (n = 5 independent samples). (d) Ratiometric fluorescence signals of DSNPs@PEI-820 *in vivo* recorded at varying laser output settings. Data are presented as mean ± SD (n = 5 independent samples). Source data are provided as a Source Data file.

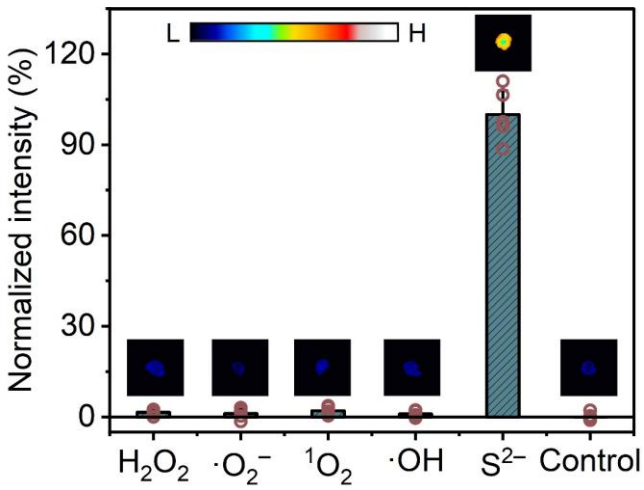

Supplementary Fig. 44. Evaluation of ROS interference on the fluorescence emission of DSNPs@PEI-820 in lettuce leaves. All ROS or their precursors were applied at a standardized concentration of 100 μM. Data are presented as mean ± SD (n = 5 independent samples). Source data are provided as a Source Data file.

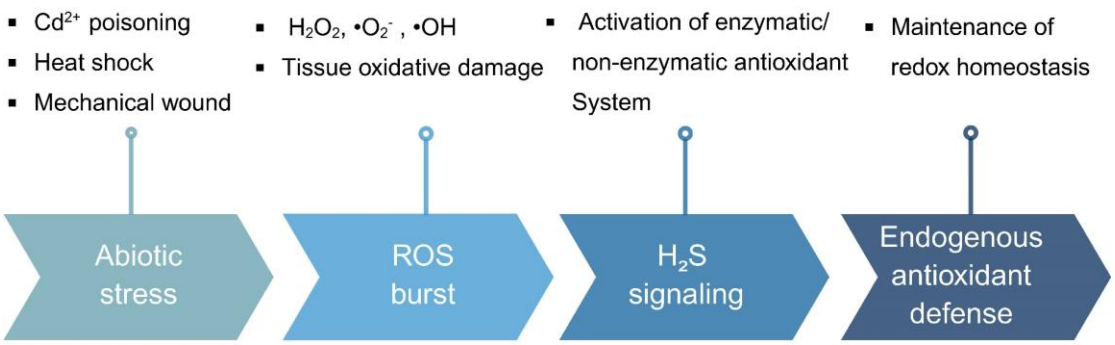

Supplementary Fig. 45. Schematic illustration of the plant response to abiotic stress through the ROS-H_2S defense pathway. Created in BioRender. Wang, Y. (2026) https://BioRender.com/t1v6apq.

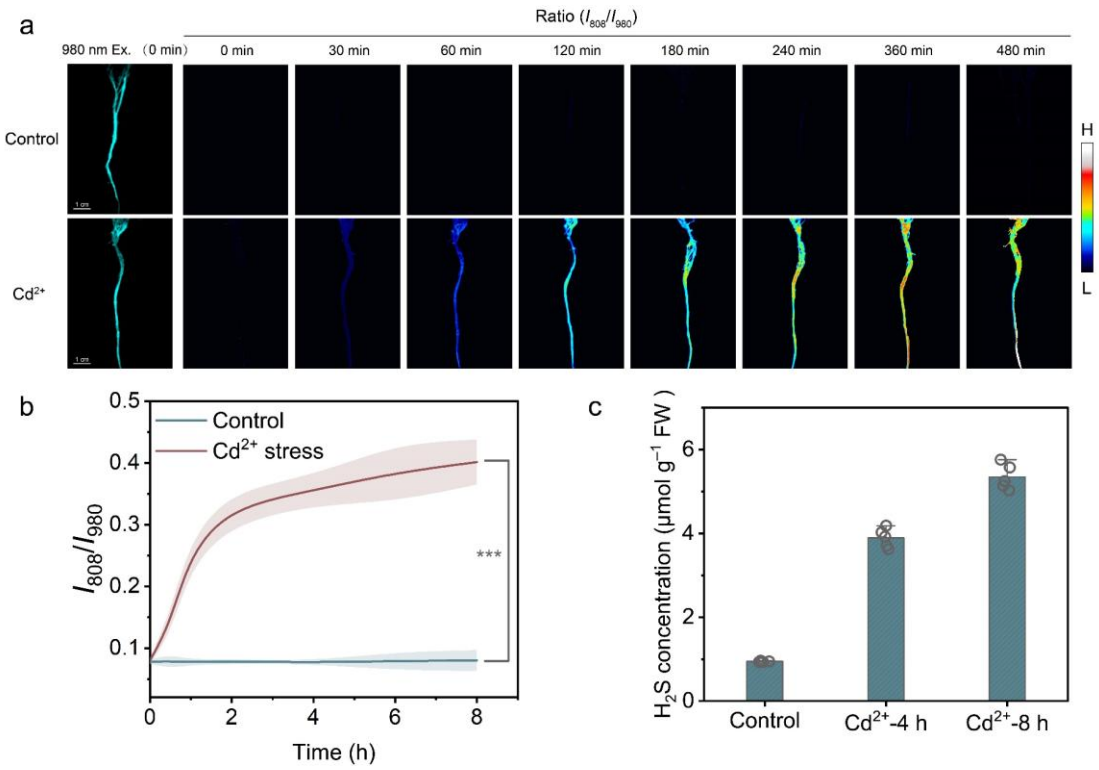

Supplementary Fig. 46. Validation of Cd^{2+}-induced H_2S dynamics in lettuce roots using DSNPs@PEI-820 delivered via root absorption. (a) Time-course NIR-IIb fluorescence images of roots under Cd^{2+} stress. Representative images from five independent biological replicates are shown, with similar results obtained in all replicates. (b) Corresponding time-dependent ratiometric fluorescence intensity curves. Data are presented as mean ± SD (n = 5 independent samples), with shaded regions indicating the SD of the ratiometric signal intensity. Statistical analysis was performed using one-way ANOVA followed by Tukey's multiple comparison test to evaluate intergroup differences (*P < 0.05, **P < 0.01, ***P < 0.001). (c) Quantification of endogenous H_2S levels in roots at different stress durations using a standard biochemical assay. Data are presented as mean ± SD (n = 5 independent samples). Source data are provided as a Source Data file.

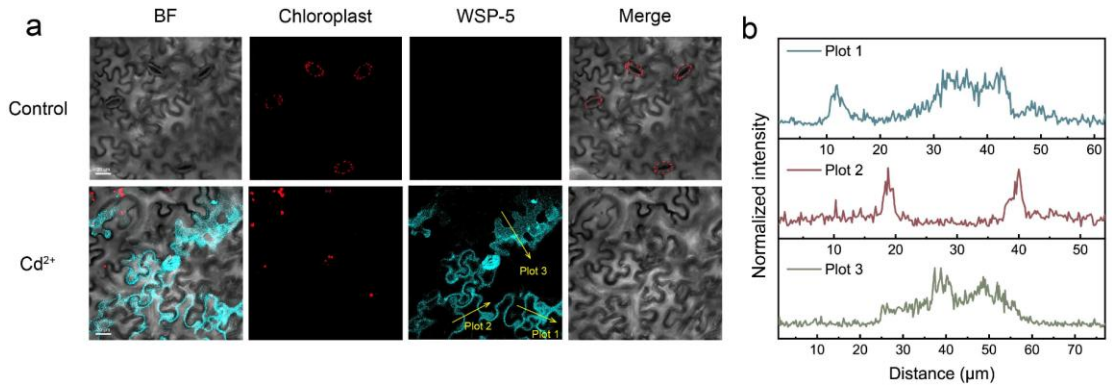

Supplementary Fig. 47. Spatial distribution of H_2S molecules in lettuce leaf tissues under Cd^{2+} stress using WSP-5. (a) Confocal images showing the intracellular and extracellular distribution of H_2S molecules in lettuce leaf tissues under Cd^{2+} stress. Representative images from five independent biological replicates are shown, with similar results obtained in all replicates. (b) Fluorescence intensity profiles along the scanning direction corresponding to the plot in panel (a). Source data are provided as a Source Data file.

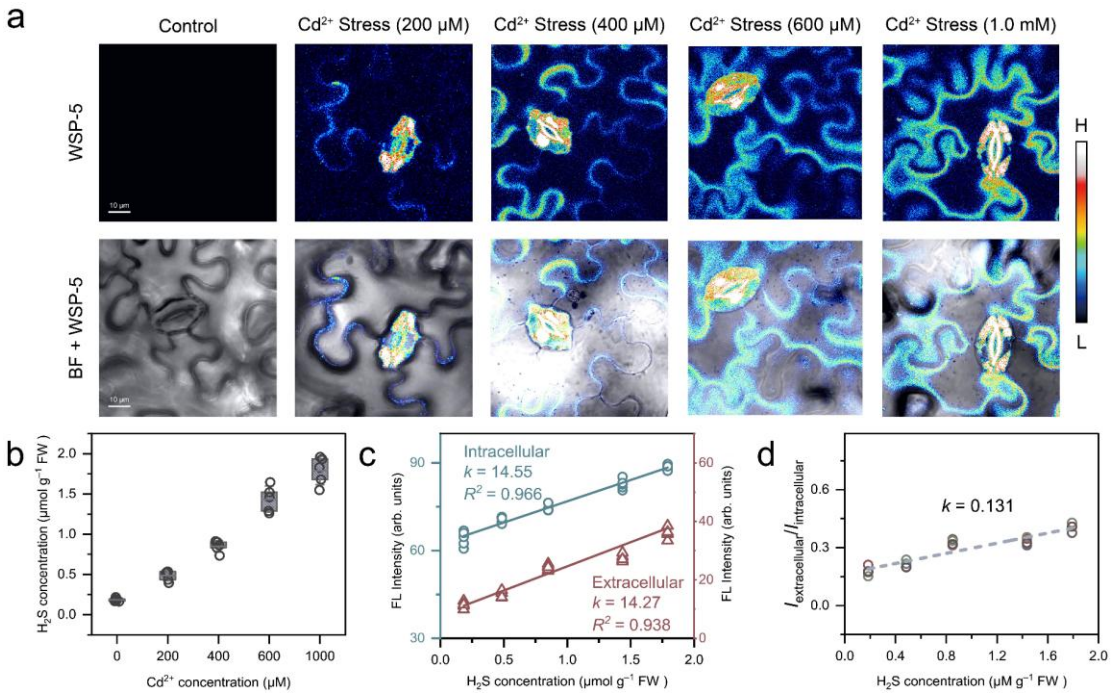

Supplementary Fig. 48. Semi-quantitative analysis of intracellular and extracellular H_2S dynamics in lettuce leaf tissues under Cd^{2+} stress. (a) Confocal fluorescence images showing the spatial distribution of intracellular and extracellular H_2S in leaf tissues under varying Cd^{2+} concentrations, using WSP-5. Representative images from five independent biological replicates are shown, with similar results obtained in all replicates. (b) Quantitative relationship between total tissue H_2S concentration and applied Cd^{2+} stress levels. Data are presented as mean ± SD (n = 5 independent samples). (c) Linear correlation between intracellular and extracellular relative fluorescence intensities and total endogenous H_2S concentration. Data are presented as individual points (n = 5 independent samples). (d) Linear relationship between the extracellular-to-intracellular signal intensity ratio and endogenous H_2S concentration. Data are presented as individual points (n = 5 independent samples). Source data are provided as a Source Data file.

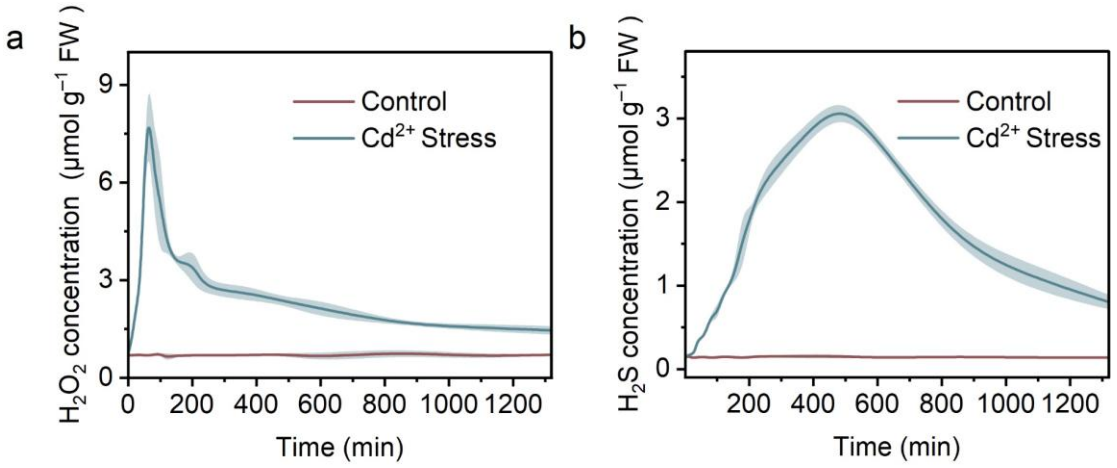

Supplementary Fig. 49. Time-dependent changes in endogenous H_2O_2 and H_2S accumulation in lettuce leaves under Cd^{2+} stress measured by colorimetric assays. (a) Time-dependent evaluation of endogenous H_2O_2 accumulation in lettuce leaves under Cd^{2+} stress. Data are presented as mean ± SD (n = 5 independent samples), with shaded regions indicating the SD of the measured concentration. (b) Time-dependent evaluation of endogenous H_2S accumulation in lettuce leaves under Cd^{2+} stress. Data are presented as mean ± SD (n = 5 independent samples), with shaded regions indicating the SD of the measured concentration. Source data are provided as a Source Data file.

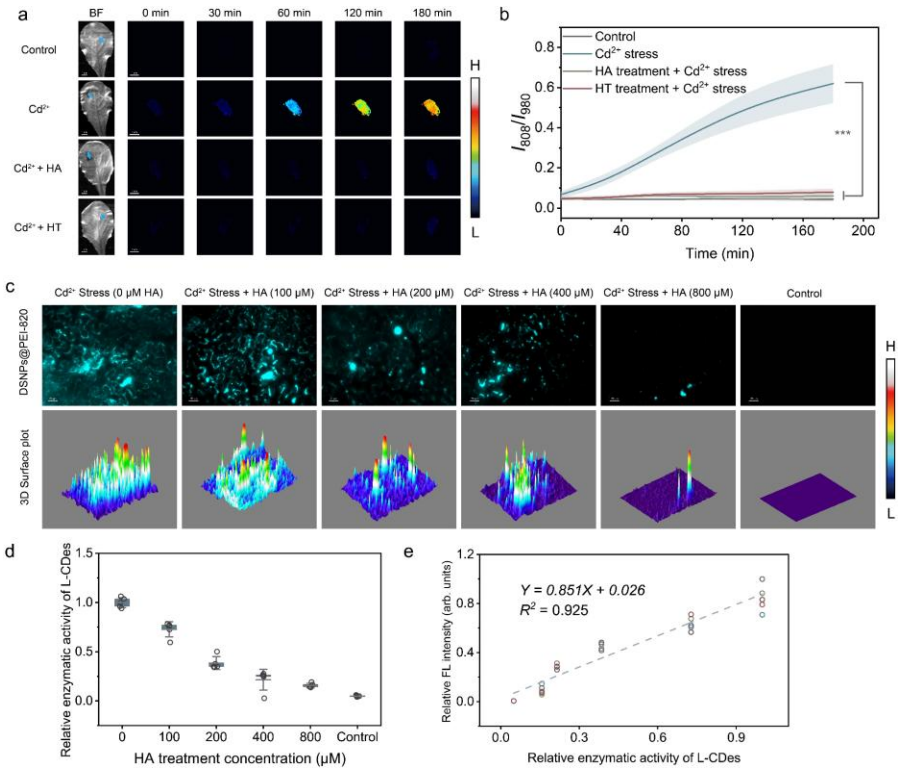

Supplementary Fig. 50. Biochemical validation of the *in vivo* specificity of DSNPs@PEI-820 toward endogenous H_2S under Cd^{2+} stress. (a) Fluorescence images of DSNPs@PEI-820 in leaves subjected to different treatments. The blue shaded areas in the BF images indicate the probe-injected regions. Representative images from five independent biological replicates are shown, with similar results obtained in all replicates. (b) Time-dependent continuous tracking of the ratiometric fluorescence signals corresponding to the experimental groups in (a). Data are presented as mean ± SD (n = 5 independent samples), with shaded regions indicating the SD of the ratiometric signal intensity. Statistical analysis was performed using one-way ANOVA followed by Tukey's multiple comparison test to evaluate intergroup differences (*P < 0.05, **P < 0.01, ***P < 0.001). (c) Fluorescence images and corresponding 3D surface intensity plots of DSNPs@PEI-820 in Cd^{2+}-stressed leaf tissues treated with varying concentrations of HA. Representative images from five independent biological replicates are shown, with similar results obtained in all replicates. (d) Quantitative relationship between the relative enzymatic activity of L-CDes and HA treatment concentration. (e) Linear correlation between the normalized fluorescence intensity of DSNPs@PEI-820 and the relative enzymatic activity of L-CDes. Data are presented as individual points (n = 5 independent samples). Source data are provided as a Source Data file.

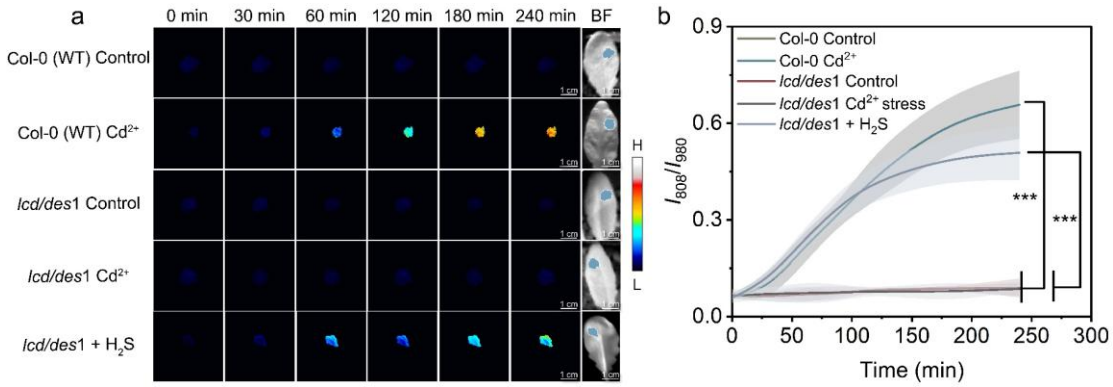

Supplementary Fig. 51. Specificity assessment of DSNPs@PEI-820 for H_2S response in wild-type (WT, Col-0) and *lcd/des1* double mutant *Arabidopsis thaliana* under Cd^{2+} stress. (a) NIR-IIb fluorescence imaging of DSNPs@PEI-820 in wild-type and *lcd/des1* double mutant *Arabidopsis thaliana* under Cd^{2+} stress. The blue shaded areas in the BF images indicate the probe-injected regions. Representative images from five independent biological replicates are shown, with similar results obtained in all replicates. (b) Time-dependent fluorescence intensity curves of DSNPs@PEI-820 in wild-type and *lcd/des1* double mutant *Arabidopsis thaliana* under Cd^{2+} stress. Data are presented as mean ± SD (n = 5 independent samples), with shaded regions indicating the SD of the ratiometric signal intensity. Statistical analysis was performed using one-way ANOVA followed by Tukey's multiple comparison test to evaluate intergroup differences (*P < 0.05, **P < 0.01, ***P < 0.001). Source data are provided as a Source Data file.

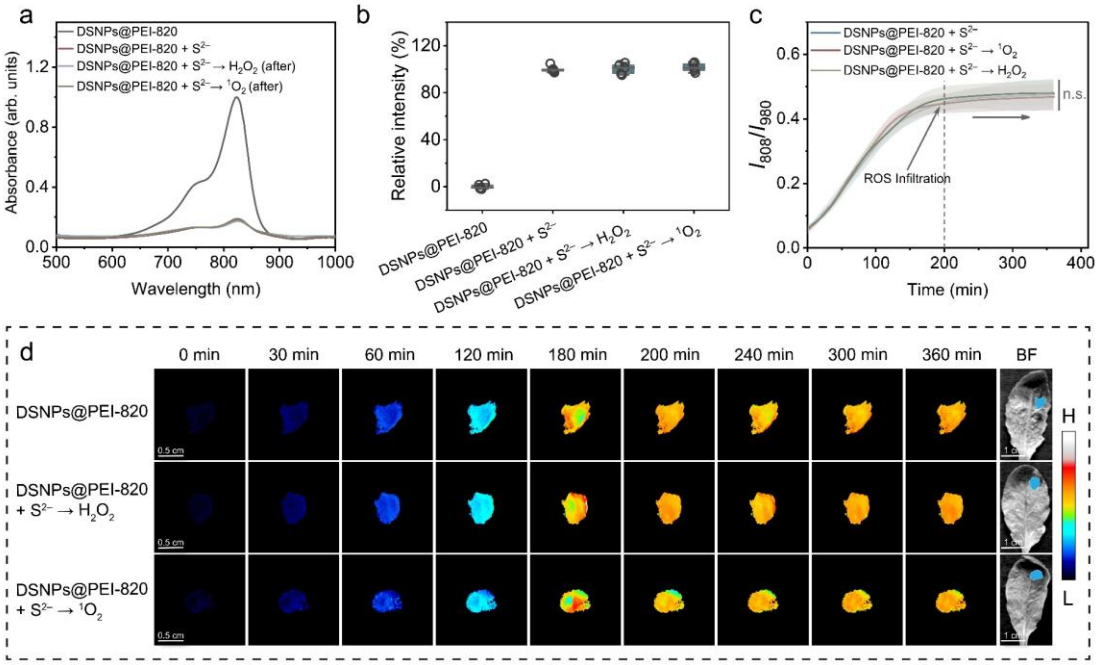

Supplementary Fig. 52. Evaluation of nanoprobe chemical stability against subsequent ROS exposure following H_2S activation. (a) Absorbance spectra of DSNPs@PEI-820 in the unreacted state, after reaction with S^{2-}, and following sequential co-incubation with H_2O_2 or $^1O_2$. (b) Relative fluorescence intensities of the nanoprobe *in vitro* under the corresponding sequential treatment conditions described in (a). Data are presented as mean ± SD (n = 5 independent samples). (c, d) *In vivo* continuous tracking of ratiometric fluorescence signals (c) and the corresponding time-course NIR-II ratiometric fluorescence images (d) in the leaves of the *lcd/des1* double mutant *Arabidopsis thaliana*. For these assays, exogenous H_2S was pre-infiltrated to establish a signal plateau, followed by secondary *in situ* infiltration of H_2O_2 or $^1O_2$ to assess signal stability. Data in (c) are presented as mean ± SD (n = 5 independent samples), with shaded regions indicating the SD of the ratiometric signal intensity. The blue shaded areas in the BF images (d) indicate the probe-injected regions. Representative images from five independent biological replicates are shown, with similar results obtained in all replicates. Statistical analysis was performed using one-way ANOVA followed by Tukey's multiple comparison test to evaluate intergroup differences (*P < 0.05, **P < 0.01, ***P < 0.001). Source data are provided as a Source Data file.

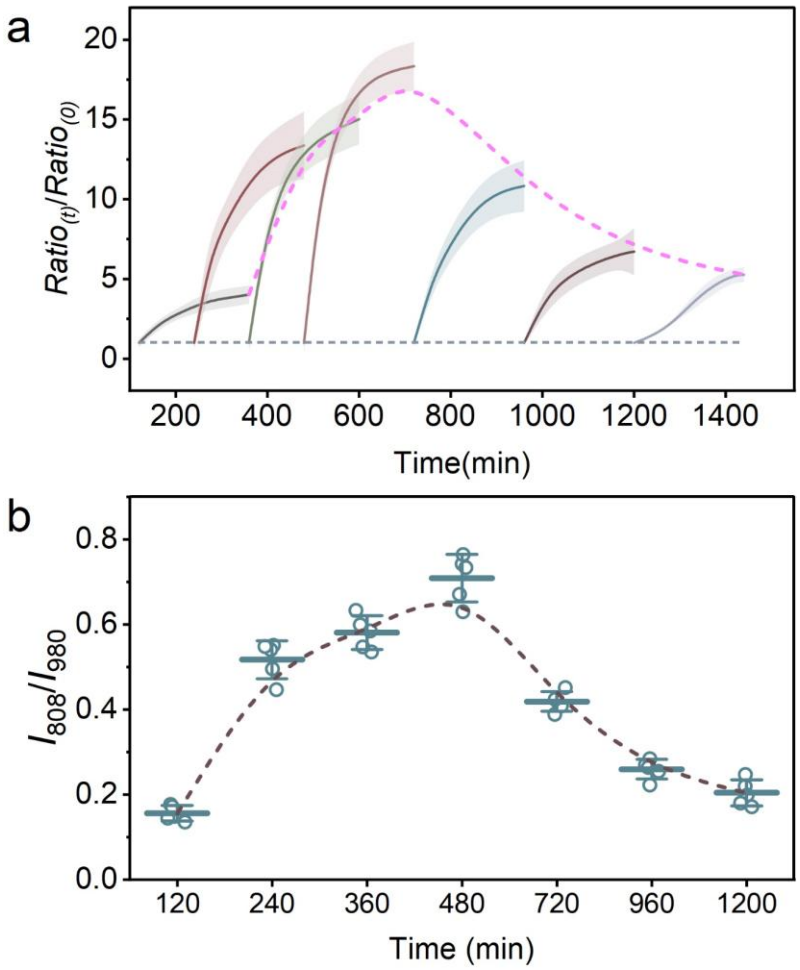

Supplementary Fig. 53. *In vivo* validation of the temporal compatibility between DSNPs@PEI-820 reaction kinetics and physiological H_2S dynamics. (a) *In vivo* reaction kinetic curves of DSNPs@PEI-820 responding to endogenous H_2S at multiple distinct time points during Cd^{2+} exposure. Data are presented as mean ± SD (n = 5 independent samples), with shaded regions indicating the SD of the intensity. (b) Reconstructed temporal profile of Cd^{2+} stress–induced H_2S dynamics based on plateau ratiometric fluorescence signals measured at different time points. Each data point represents the steady-state signal obtained after an independent nanoprobe injection at the corresponding time point. Data are presented as mean ± SD (n = 5 independent samples). Source data are provided as a Source Data file.

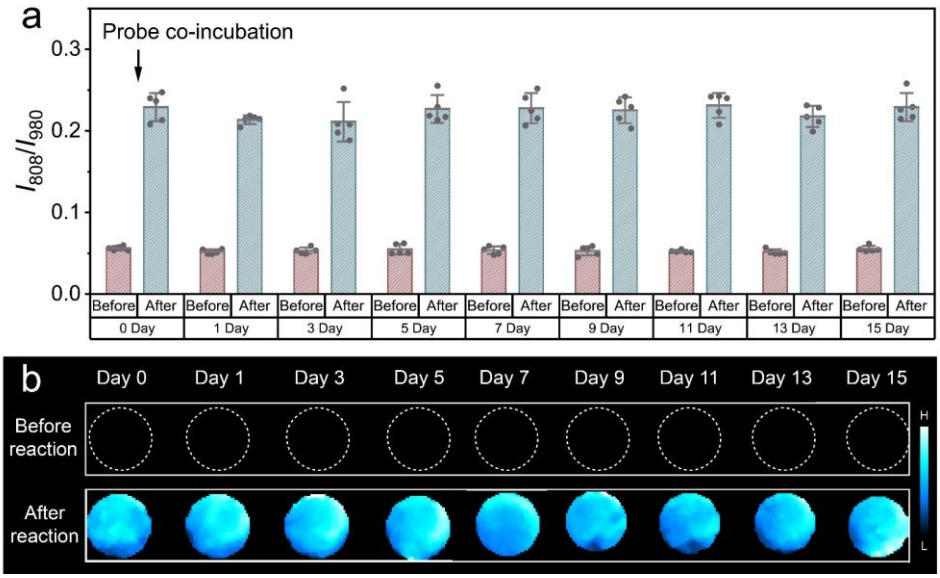

Supplementary Fig. 54. Long-term functional stability and sensing reliability of DSNPs@PEI-820 for continuous *in vitro* monitoring. (a) Ratiometric fluorescence responses of DSNPs@PEI-820 to S^{2-} measured at specific time points during a 15-day continuous co-incubation within a simulated leaf tissue matrix. Data are presented as mean ± SD (n = 5 independent samples). (b) Corresponding NIR-II ratiometric fluorescence images. Representative images from five independent biological replicates are shown, with similar results obtained in all replicates. Source data are provided as a Source Data file.

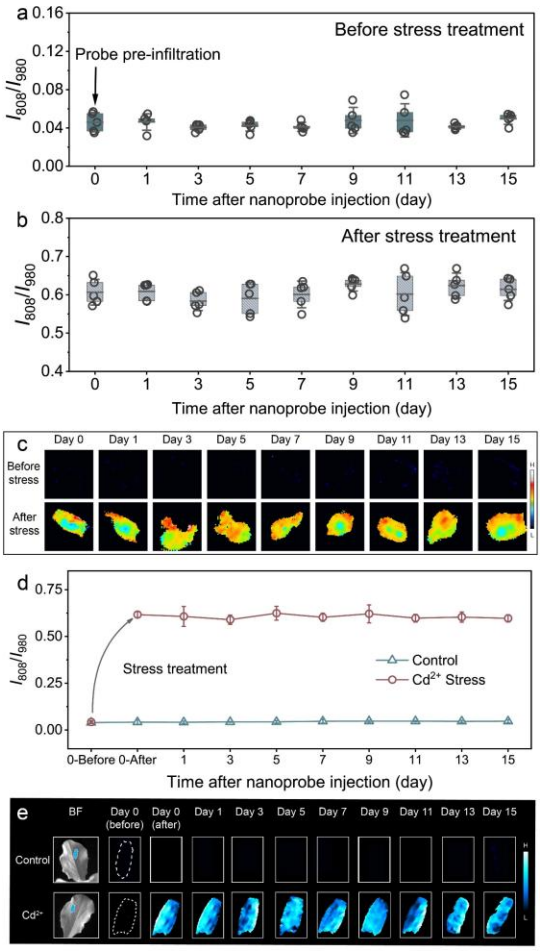

Supplementary Fig. 55. *In vivo* long-term signal stability and sensing reliability of DSNPs@PEI-820 in lettuce leaves. (a) Baseline stability of the nanoprobe, measured prior to stress induction on each designated day. Data are presented as mean ± SD (n = 5 independent samples). (b) Ratiometric fluorescence responses recorded after stress induction on the corresponding designated days. Data are presented as mean ± SD (n = 5 independent samples). (c) Representative *in vivo* NIR-II ratiometric fluorescence images corresponding to panels (a) and (b). Representative images from five independent biological replicates are shown, with similar results obtained in all replicates. (d) Long-term signal retention profile tracked continuously over a 15-day period following a single stress activation on Day 0. Data are presented as mean ± SD (n = 5 independent samples). (e) Corresponding time-course images for panel (d), comparing the control and Cd^{2+} stress groups. The blue shaded areas in the BF images indicate the probe-injected regions. Representative images from five independent biological replicates are shown, with similar results obtained in all replicates. Source data are provided as a Source Data file.

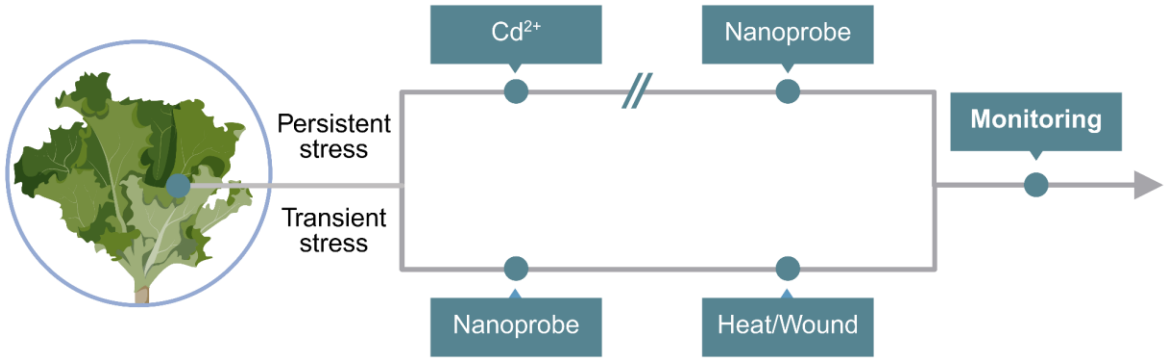

Supplementary Fig. 56. Schematic diagram illustrating the operational procedure for *in situ* monitoring of plant stress-induced H_2S using DSNPs@PEI-820 nanoprobes. Created in BioRender. Feng, J. (2026) https://BioRender.com/mil8qrt.

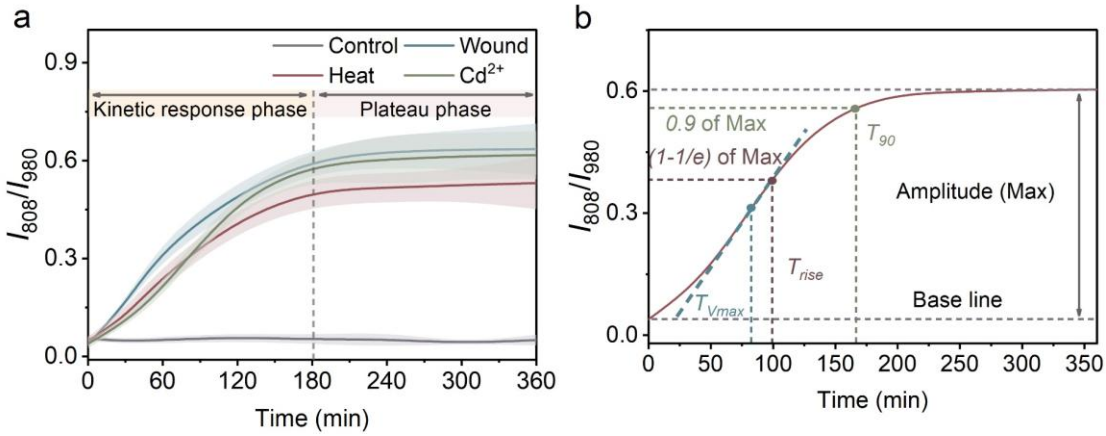

Supplementary Fig. 57. Extended *in vivo* NIR-IIb monitoring and kinetic parameter extraction of stress-induced H_2S dynamics using DSNPs@PEI-820. (a) Time-dependent fluorescence responses of lettuce leaves under wounding, heat shock, and Cd^{2+} stress conditions, monitored by DSNPs@PEI-820 over a 6 h period. Data are presented as mean ± SD (n = 5 independent samples), with shaded regions indicating the SD of the ratiometric signal intensity. (b) Schematic illustration of the kinetic parameters extracted from the DSNPs@PEI-820 response signals under different stress conditions. Amplitude (Max): The final plateau height reached by the cumulative signal[40]. V_{max} and T_{max}: V_{max} is the maximum tangent slope on the curve, representing the peak apparent reaction rate between the probe and H_2S during the stress response; T_{max} is the corresponding time point. V_{rise} and T_{rise}: The rate and time corresponding to when the signal reaches $1-1/e$ of the amplitude[41]. T_{90} and V_{90}: T_{90} is the time required for the signal to reach 0.9 of the amplitude, and V_{90} represents the dynamic reaction rate at this specific time point[42–44]. Source data are provided as a Source Data file.

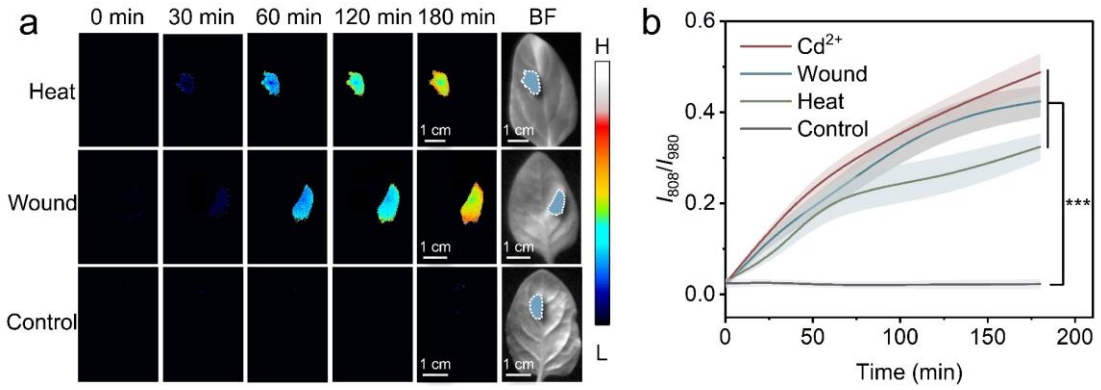

Supplementary Fig. 58. *In situ* imaging of endogenous H_2S production induced by different abiotic stresses in spinach using DSNPs@PEI-820. (a) NIR-IIb imaging of stressed spinach with DSNPs@PEI-820. Pseudo-colors were applied to regions with significant fluorescence signals to differentiate the intensity. The blue shaded areas in the BF images indicate the probe-injected regions. Representative images from five independent biological replicates are shown, with similar results obtained in all replicates. (b) Temporal response curve of endogenous H_2S production in spinach under heat shock and mechanical wounding stress, monitored by DSNPs@PEI-820. Data are presented as mean ± SD (n = 5 independent samples), with shaded regions indicating the SD of the ratiometric signal intensity. Statistical analysis was performed using one-way ANOVA followed by Tukey's multiple comparison test to evaluate intergroup differences (*P < 0.05, **P < 0.01, ***P < 0.001). Source data are provided as a Source Data file.

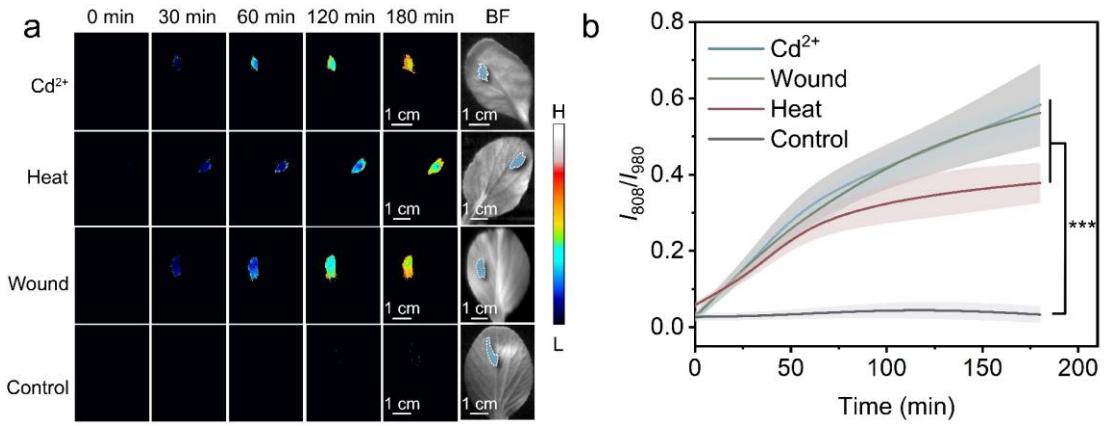

Supplementary Fig. 59. *In situ* imaging of endogenous H_2S production induced by different abiotic stresses in pak choi using DSNPs@PEI-820. (a) NIR-IIb imaging of stressed pak choi with DSNPs@PEI-820. Pseudo-colors were applied to regions with significant fluorescence signals to differentiate the intensity. The blue shaded areas in the BF images indicate the probe-injected regions. Representative images from five independent biological replicates are shown, with similar results obtained in all replicates. (b) Temporal response curve of endogenous H_2S production in pak choi under heat shock, mechanical wounding, and Cd^{2+}stress, monitored by DSNPs@PEI-820. Data are presented as mean ± SD (n = 5 independent samples), with shaded regions indicating the SD of the ratiometric signal intensity. Statistical analysis was performed using one-way ANOVA followed by Tukey's multiple comparison test to evaluate intergroup differences (*P < 0.05, **P < 0.01, ***P < 0.001). Source data are provided as a Source Data file.

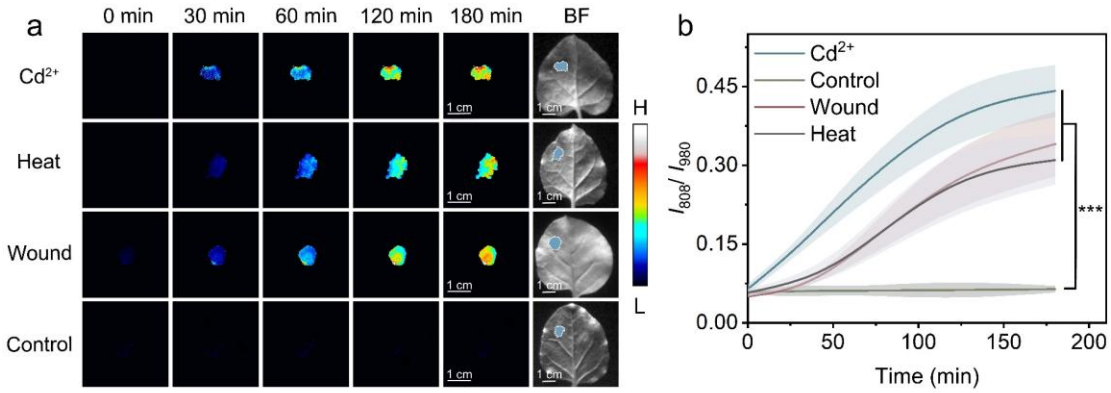

Supplementary Fig. 60. *In situ* imaging of endogenous H_2S production induced by different abiotic stresses in tobacco using DSNPs@PEI-820. (a) NIR-IIb imaging of stressed tobacco with DSNPs@PEI-820. Pseudo-colors were applied to regions with significant fluorescence signals to differentiate the intensity. The blue shaded areas in the BF images indicate the probe-injected regions. Representative images from five independent biological replicates are shown, with similar results obtained in all replicates. (b) Temporal response curve of endogenous H_2S production in tobacco under heat shock, mechanical wounding and Cd^{2+}stress, monitored by DSNPs@PEI-820. Data are presented as mean ± SD (n = 5 independent samples), with shaded regions indicating the SD of the ratiometric signal intensity. Statistical analysis was performed using one-way ANOVA followed by Tukey's multiple comparison test to evaluate intergroup differences (*P < 0.05, **P < 0.01, ***P < 0.001). Source data are provided as a Source Data file.

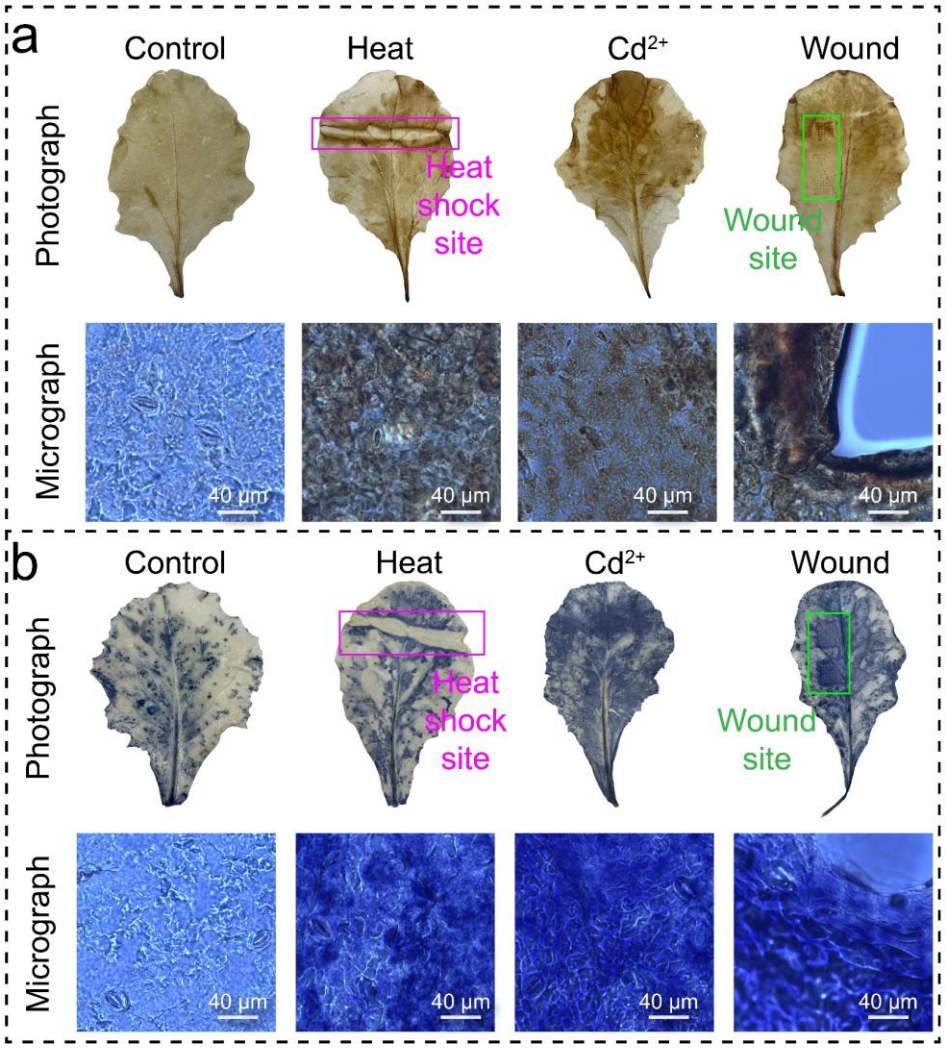

Supplementary Fig. 61. ROS staining of lettuce leaves subjected to various abiotic stresses. Representative optical and microscopic photographs of DAB staining (a) and NBT staining (b) of lettuce leaves subjected to different abiotic stresses. The purple and green boxes indicate the damaged areas. Representative images from five independent biological replicates are shown, with similar results obtained in all replicates.

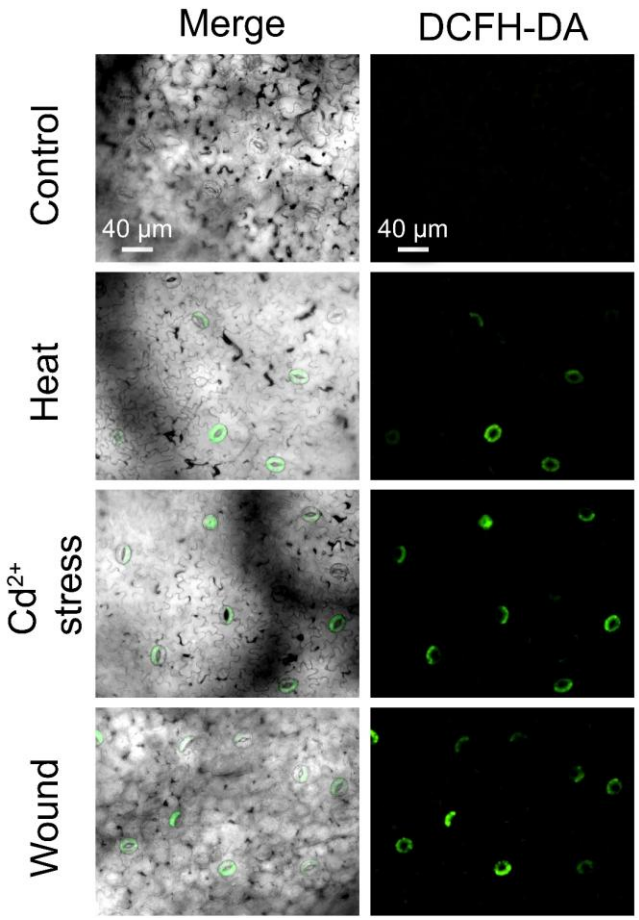

Supplementary Fig. 62. Fluorescent images of DCFH-DA-stained lettuce subjected to various abiotic stresses. Representative images from five independent biological replicates are shown, with similar results obtained in all replicates.

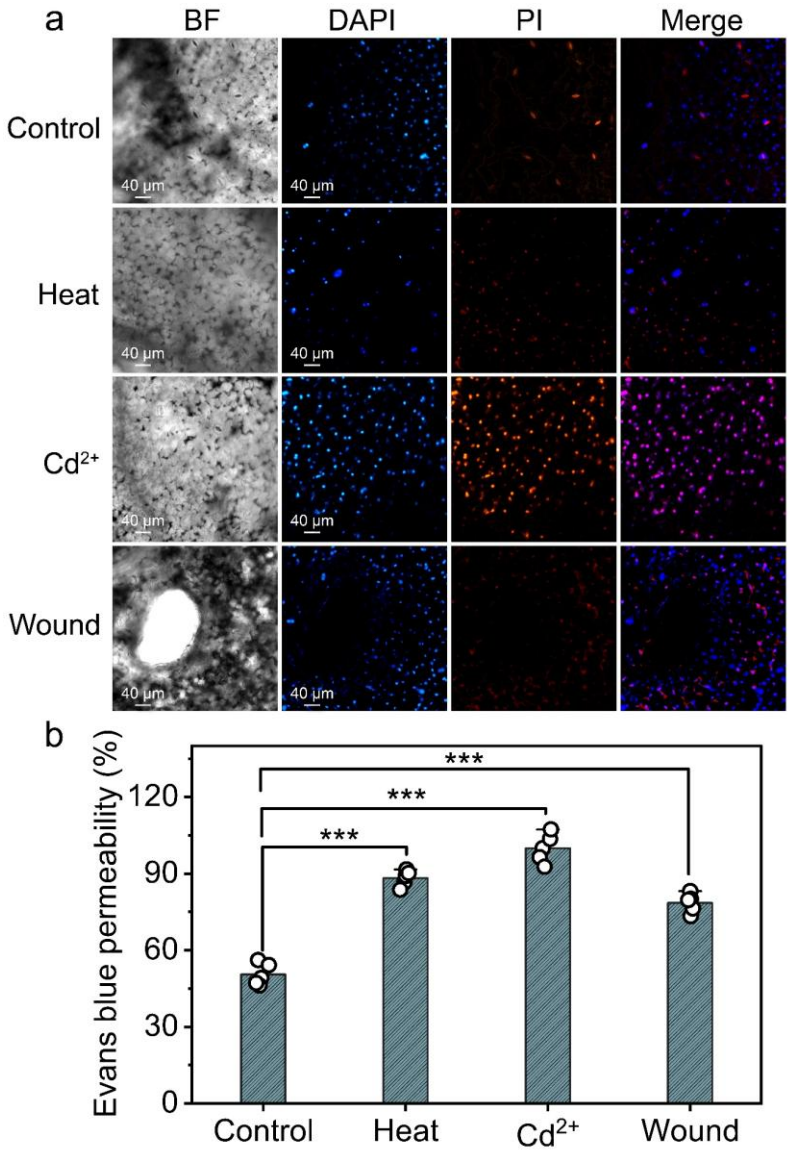

Supplementary Fig. 63. Assessment of cellular viability and membrane integrity in lettuce leaf tissues subjected to various abiotic stresses. (a) Representative fluorescent images of DAPI/PI live/dead cell staining of lettuce leaf tissue subjected to different abiotic stresses. Representative images from five independent biological replicates are shown, with similar results obtained in all replicates. (b) Evans blue staining results for lettuce leaf tissues under different abiotic stress conditions. Data are presented as mean ± SD (n = 5 independent samples). Statistical analysis was performed using one-way ANOVA followed by Tukey's multiple comparison test to evaluate intergroup differences (*P < 0.05, **P < 0.01, ***P < 0.001). Source data are provided as a Source Data file.

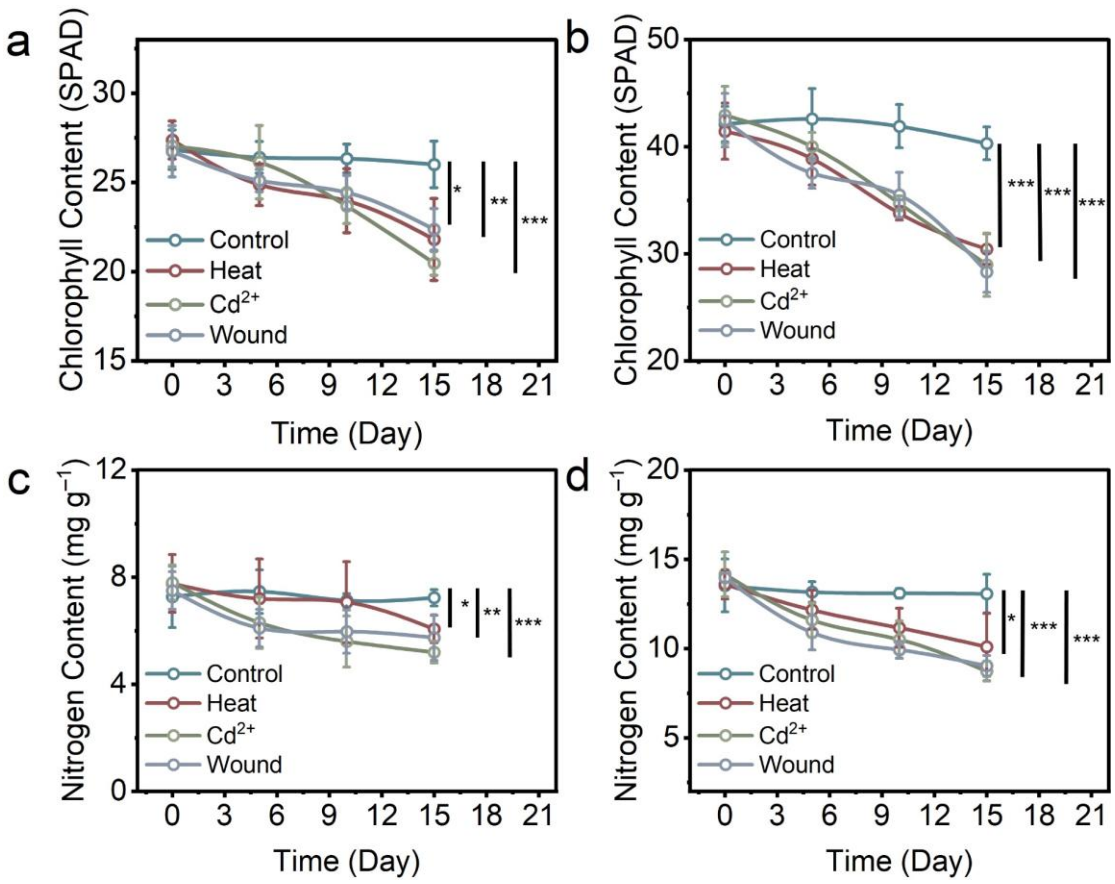

Supplementary Fig. 64. Changes in chlorophyll and nitrogen content in lettuce and spinach leaves under various abiotic stress conditions. Leaf chlorophyll content profiles of lettuce (a) and spinach (b) under different abiotic stresses. Profiles of leaf nitrogen content in lettuce (c) and spinach (d) under different abiotic stresses. Data are presented as mean ± SD (n = 5 independent samples). Statistical analysis was performed using one-way ANOVA followed by Tukey's multiple comparison test to evaluate intergroup differences (*$P < 0.05$, **$P < 0.01$, ***$P < 0.001$).

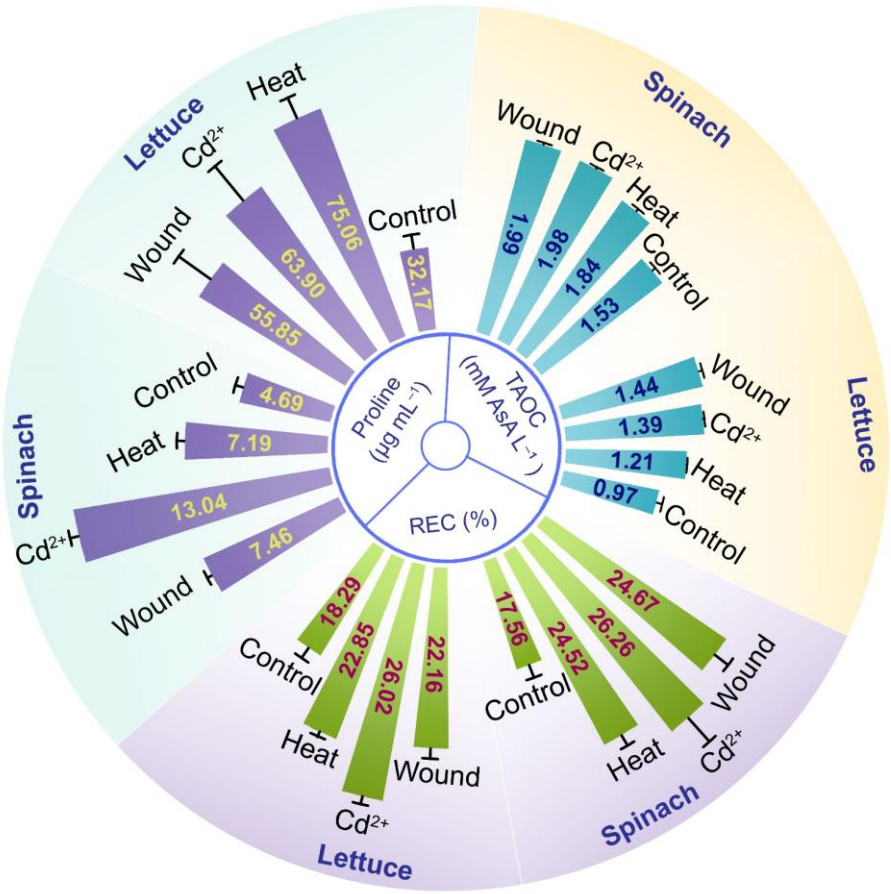

Supplementary Fig. 65. REC, TAOC, and proline levels in lettuce and spinach under different stress conditions. The data are presented as mean ± SD (n = 5 independent samples). Source data are provided as a Source Data file.

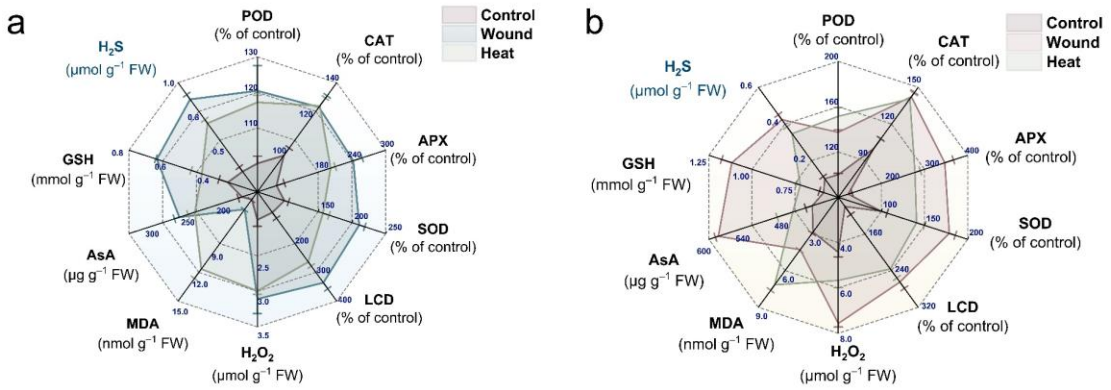

Supplementary Fig. 66. Assessment of oxidative stress biomarkers in lettuce and spinach under mechanical wounding and heat shock. Response profiles of enzymatic and non-enzymatic antioxidant systems to heat shock and mechanical wounding in lettuce (a) and spinach (b). Data are presented as mean ± SD (n = 5 independent samples). Source data are provided as a Source Data file.

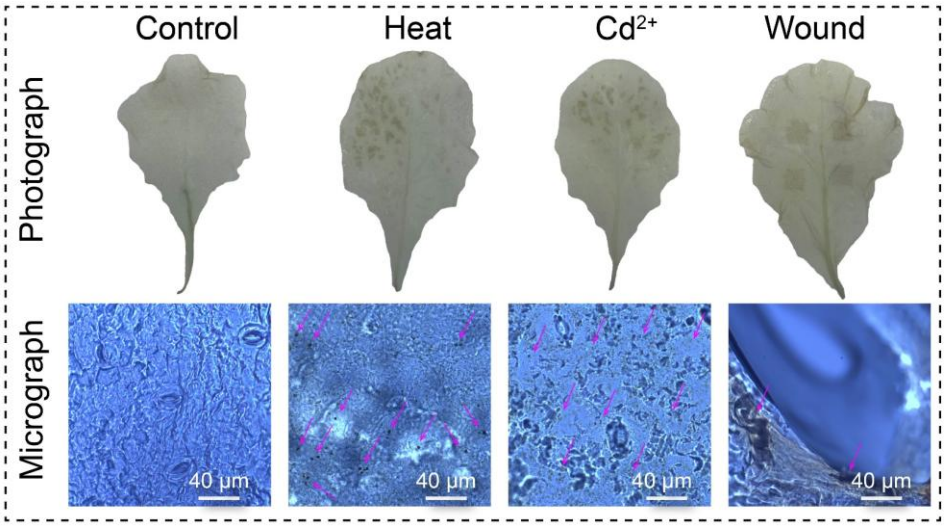

Supplementary Fig. 67. Representative photographs and micrographs of Cu^{2+} staining for H_2S in lettuce leaf tissues subjected to different abiotic stresses. The pink arrows highlight the localization of endogenous H_2S within the leaf tissues. Representative images from five independent biological replicates are shown, with similar results obtained in all replicates.

Supplementary Table 1. Summary of representative multiparametric kinetic indicators extracted from *in vivo* NIR-IIb fluorescence monitoring of various abiotic stresses in lettuce leaves using DSNPs@PEI-820.

Stress	Amplitude (intensity)	T_{vmax} (min)	T_{rise} (min)	T_{90} (min)	V_{max} (10^{-3} min^{-1})	V_{rise} (10^{-3} min^{-1})	V_{90} (10^{-3} min^{-1})
Wound	0.62 ± 0.023	34.83 ± 3.06	92.76 ± 8.94	170.79 ± 5.29	4.84 ± 0.31	3.40 ± 0.39	0.82 ± 0.14
Heat shock	0.51 ± 0.018	67.84 ± 7.45	92.10 ± 2.63	163.96 ± 8.34	3.24 ± 0.56	3.37 ± 0.34	0.81 ± 0.097
Cd^{2+}	0.61 ± 0.016	79.01 ± 9.45	107.40 ± 6.67	157.98 ± 11.35	4.76 ± 0.6	4.70 ± 0.65	1.56 ± 0.22

Data are presented as mean ± SD (n = 5 independent samples).

Supplementary references

1. Han, S. *et al.* Lanthanide-doped inorganic nanoparticles turn molecular triplet excitons bright. *Nature* **587**, 594–599 (2020).

2. Liu, Q., Zhong, Y., Su, Y., Zhao, L. & Peng, J. Real-time imaging of hepatic inflammation using hydrogen sulfide-activatable second near-infrared luminescent nanoprobes. *Nano Lett.* **21**, 4606–4614 (2021).

3. Rivero, R. M. *et al.* Delayed leaf senescence induces extreme drought tolerance in a flowering plant. *Proc. Natl. Acad. Sci.* **104**, 19631–19636 (2007).

4. Shi, H. *et al.* Hydrogen sulfide regulates abiotic stress tolerance and biotic stress resistance in *Arabidopsis*. *J. Integr. Plant Biol.* **57**, 628–640 (2015).

5. Nasiri, M. *et al.* Enhancing salt stress tolerance in kidney beans: the synergistic effects of biochar and salicylic acid in arid and semi-arid regions. *Plant Stress* **11**, 100423 (2024).

6. Ma, N.-N. *et al.* The multiple stress-responsive transcription factor *SlNAC1* improves the chilling tolerance of tomato. *Physiol. Plant.* **149**, 474–486 (2013).

7. Liu, J. *et al.* Iron nanoparticle/carbon nanotube composite as oxidase-like nanozyme for visual analysis of total antioxidant capacity. *Food Chem.: X* **25**, 102093 (2025).

8. Lou, Z., Zhao, S., Wang, Q. & Wei, H. N-doped carbon As peroxidase-like nanozymes for total antioxidant capacity assay. *Anal. Chem.* **91**, 15267–15274 (2019).

9. Riemenschneider, A., Nikiforova, V., Hoefgen, R., De Kok, L. J. & Papenbrock, J. Impact of elevated H_2S on metabolite levels, activity of enzymes and expression of genes involved in cysteine metabolism. *Plant Physiol. Biochem.* **43**, 473–483 (2005).

10. Corpas, F. J., Barroso, J. B., González-Gordo, S., Muñoz-Vargas, M. A. & Palma, J. M. Hydrogen sulfide: a novel component in *Arabidopsis* peroxisomes which triggers catalase inhibition. *J. Integr. Plant Biol.* **61**, 871–883 (2019).

11. Zhang, R. *et al.* Edge-site engineering of defective Fe–N_4 nanozymes with boosted catalase-like performance for retinal vasculopathies. *Adv. Mater.* **34**, 2270275 (2022).

12. Jürgen-Lohmann, D. L. & Legge, R. L. Immobilization of bovine catalase in sol–gels. *Enzyme Microb. Technol.* **39**, 626–633 (2006).

13. Abass, M. & Morris, P. C. The hordeum vulgare signalling protein MAP kinase 4 is a regulator of biotic and abiotic stress responses. *J. Plant Physiol.* **170**, 1353–1359 (2013).

14. Barceló, A. Hydrogen peroxide production is a general property of the lignifying xylem from vascular plants. *Ann. Bot.* **82**, 97–103 (1998).

15. Johnsen, A. R. & Jacobsen, O. S. A quick and sensitive method for the quantification of peroxidase activity of organic surface soil from forests. *Soil Biol. Biochem.* **40**, 814–821 (2008).

16. Rossetti, S. & Bonatti, P. M. *In situ* histochemical monitoring of ozone- and TMV-induced reactive oxygen species in tobacco leaves. *Plant Physiol. Biochem.* **39**, 433–442 (2001).

17. Romero-Puertas, M. C. *et al.* Cadmium-induced subcellular accumulation of O_2^- and H_2O_2 in pea leaves. *Plant Cell Environ.* **27**, 1122–1134 (2004).

18. Kwak, S.-Y. *et al.* Chloroplast-selective gene delivery and expression in planta using chitosan-complexed single-walled carbon nanotube carriers. *Nat. Nanotechnol.* **14**, 447–455 (2019).

19. Demirer, G. S. *et al.* High aspect ratio nanomaterials enable delivery of functional genetic material without DNA integration in mature plants. *Nat. Nanotechnol.* **14**, 456–464 (2019).

20. Son, W. K. *et al. In vivo* surface-enhanced raman scattering nanosensor for the real-time monitoring of multiple stress signalling molecules in plants. *Nat. Nanotechnol.* **18**, 205–216 (2023).

21. Neese, F. The SHARK integral generation and digestion system. *J. Comput. Chem.* **44**, 381–396 (2023).

22. Neese, F. Software update: the ORCA program system—version 5.0. *WIREs Comput. Mol. Sci.* **12**, e1606 (2022).

23. Neese, F. An improvement of the resolution of the identity approximation for the formation of the coulomb matrix. *J. Comput. Chem.* **24**, 1741–1747 (2003).

24. Neese, F., Wennmohs, F., Hansen, A. & Becker, U. Efficient, approximate and parallel hartree–fock and hybrid DFT calculations. A 'chain-of-spheres' algorithm for the hartree–fock exchange. *Chem. Phys.* **356**, 98–109 (2009).

25. Grimme, S., Ehrlich, S. & Goerigk, L. Effect of the damping function in dispersion corrected density functional theory. *J. Comput. Chem.* **32**, 1456–1465 (2011).

26. Grimme, S., Antony, J., Ehrlich, S. & Krieg, H. A consistent and accurate *ab initio* parametrization of density

functional dispersion correction (DFT-D) for the 94 elements H-Pu. *J. Chem. Phys.* **132**, 154104 (2010).

27. Weigend, F. & Ahlrichs, R. Balanced basis sets of split valence, triple zeta valence and quadruple zeta valence quality for H to Rn: design and assessment of accuracy. *Phys. Chem. Chem. Phys.* **7**, 3297 (2005).

28. Marenich, A. V., Cramer, C. J. & Truhlar, D. G. Universal solvation model based on solute electron density and on a continuum model of the solvent defined by the bulk dielectric constant and atomic surface tensions. *J. Phys. Chem. B* **113**, 6378–6396 (2009).

29. Lu, T. A comprehensive electron wavefunction analysis toolbox for chemists, multiwfn. *J. Chem. Phys.* **161**, 82503 (2024).

30. Lu, T. & Chen, F. Multiwfn: a multifunctional wavefunction analyzer. *J. Comput. Chem.* **33**, 581–592 (2012).

31. Humphrey, W., Dalke, A. & Schulten, K. VMD: visual molecular dynamics. *J. Mol. Graphics* **14**, 33–38 (1996).

32. Momma, K. & Izumi, F. *VESTA 3* for three-dimensional visualization of crystal, volumetric and morphology data. *J. Appl. Crystallogr.* **44**, 1272–1276 (2011).

33. Donaldson, L. Autofluorescence in plants. *Molecules* **25**, 2393 (2020).

34. Xu, K. & Ye, H. Light scattering in stacked mesophyll cells results in similarity characteristic of solar spectral reflectance and transmittance of natural leaves. *Sci. Rep.* **13**, 4694 (2023).

35. Feret, J.-B. *et al.* PROSPECT-4 and 5: advances in the leaf optical properties model separating photosynthetic pigments. *Remote Sens. Environ.* **112**, 3031–3043 (2008).

36. Kenry, Duan, Y. & Liu, B. Recent advances of optical imaging in the second near-infrared window. *Adv. Mater.* **30**, 1802394 (2018).

37. Li, J. *et al.* High-contrast *in vivo* fluorescence imaging exploiting wavelengths beyond 1880 nm. *Nat. Commun.* **16**, 4436 (2025).

38. Routier, C., Hermida-Carrera, C. & Stavrinidou, E. Investigating the effect of syringe infiltration on *Nicotiana tabacum* (tobacco). *ACS Agric. Sci. Technol.* **5**, 28–35 (2025).

39. Chincinska, I. A. Leaf infiltration in plant science: old method, new possibilities. *Plant Methods* **17**, 83–103 (2021).

40. Lew, T. T. S. *et al.* Real-time detection of wound-induced H_2O_2 signalling waves in plants with optical

nanosensors. *Nat. Plants* **6**, 404–415 (2020).

41. Wen, H. *et al.* Mutually reinforcing and transpiration-dependent propagation of H_2O_2 and variation potential in plants revealed by fiber organic electrochemical transistors. *Innovation* **6**, 100800 (2025).

42. Cho, S.-Y. *et al.* Antibody-free rapid detection of SARS-CoV-2 proteins using corona phase molecular recognition to accelerate development time. *Anal. Chem.* **93**, 14685–14693 (2021).

43. Kuronuma, Y. *et al.* Ratiometric imaging for quantification of elevated Ca^{2+} in neurons using synthetic low-affinity fluorescent probe. *ACS Chem. Neurosci.* **16**, 649–658 (2025).

44. Ziegler, J. M. *et al.* Sensors based upon nanowires, nanotubes, and nanoribbons: 2016–2020. *Anal. Chem.* **93**, 124–166 (2021).